Thin-Walled Structures 188 (2023) 110836

Contents lists available at ScienceDirect

Thin-Walled Structures

journal homepage: www.elsevier.com/locate/tws

Full length article

Dynamic three-point bending tests under high loading rates

Tianyu Chen [a], Quanyu Jiang [a,b], Jian Xue [c], Christopher M. Harvey [d,e], Xiang Zhang [f], Vadim V. Silberschmidt [g], Yiding Liu [h], Kun Zhang [a,b,*], Simon Wang [d,e], Bingchen Wei [a,b,*]

[a] Key Laboratory of Microgravity (National Microgravity Laboratory), Institute of Mechanics, Chinese Academy of Sciences, Beijing 100190, China
[b] School of Engineering Science, University of Chinese Academy of Sciences, Beijing 100049, China
[c] State Key Laboratory of Nonlinear Mechanics, Institute of Mechanics, Chinese Academy of Sciences, Beijing 100190, China
[d] Department of Aeronautical and Automotive Engineering, Loughborough University, Loughborough, Leicestershire LE11 3TU, UK
[e] School of Mechanical and Equipment Engineering, Hebei University of Engineering, Handan 056038, China
[f] Centre for Manufacturing and Materials Engineering, Coventry University, Coventry, CV1 5FB, UK
[g] Wolfson School of Mechanical, Electrical and Manufacturing Engineering, Loughborough University, Loughborough, Leicestershire LE11 3TU, UK
[h] School of Physics, Engineering and Computer Science, University of Hertfordshire, Hatfield, Hertfordshire AL10 9AB, UK

ARTICLE INFO

Keywords:
Beam dynamics
Three-point bending test
Dynamic shear stress
Dynamic normal stress
Structural vibration

ABSTRACT

The theory of dynamic three-point bending tests under high-loading rates is developed for the first time with account for structural vibration. Analytical solutions for dynamic normal (flexural) and shear stresses are derived. To study the dynamic effect, dynamic factors for both types of stresses are defined and investigated by employing a dimensionless characteristic time and a strain rate. It is found that both dynamic factors attenuate with respect to the characteristic time and, therefore, the quasi-static time thresholds and loading conditions are obtained. In addition, the dominant failure mode is studied for potential application in brittle materials in terms of normal-to-shear stress ratio, which is oscillatory in contrast to the quasi-static case. The developed theory is verified with a split Hopkinson bar test together combined with digital image correlation as well as finite-element simulations. The findings of this study can provide a guideline for test design, such as selection of specimen geometry and loading rate. As the theory provides a modal decomposition of dynamic normal and shear stresses, it can also be used in the field of structural health monitoring.

1. Introduction

Determination of the flexural properties of materials and structures is essential for the design of thin-walled structures and assessment of related engineering structures subjected to transverse loads, and bending tests are commonly used for this purpose [1–6], for instance three-point bending. This type of tests can be employed to study the mechanical properties of materials as well as their failure modes. For brittle materials, such as carbon-fiber-reinforced plastics (CFRPs), the failure can be back fiber breakage (flexural failure) or interlaminar delamination (shear failure) [7]; for ductile materials, such as polymers and metallic alloys, bending failure can also be evaluated in terms of the flexural yield strength and flexural ultimate strength [8]. All these analyses require the accurate assessment of normal (flexural) and shear stresses for the three-point-bending configuration under transverse loads.

In a quasi-static loading regime, this configuration has been well studied and can be designed according to the purpose of the tests. For instance, by adjusting a span-to-thickness ratio $2L/h$ (where L is the half span, as shown in Fig. 1), the three-point bending configuration can be used to study the shear properties using the relationship between the maximum normal (flexural) and shear stresses $\sigma/\tau = 4L/h$ for quasi-static loads [9]. This configuration was also widely employed to assess the material properties of metallic materials [10], ceramics [11,12], polymers [13], composite materials [14–16] as well as tests of engineering structures for various sectors, such as civil engineering [17,18], aviation [19,20] and structural health monitoring [21–23]. As a result, for the quasi-static regime, several standardized testing methods were developed based on the three-point bending configuration, such as ASTM C393 [24], C1161 [25], C1609 [26], D790 [27], D2344 [28], D7264 [29], E290 [30].

In the dynamic loading regime, three-point bending was also widely used in experiments [31–36], performed with servo-hydraulic machines, as well as drop-weight and split Hopkinson bar (SHB) methods. The applied forces were usually measured and processed to derive the required mechanical parameters. A general finding was the oscillatory character of applied forces reflecting the dynamic response of the specimens. From the mechanical perspective, the dynamic response

* Corresponding author at: Key Laboratory of Microgravity (National Microgravity Laboratory), Institute of Mechanics, Chinese Academy of Sciences, Beijing 100190, China.
E-mail addresses: chentianyu@imech.ac.cn (T. Chen), zhangkun@imech.ac.cn (K. Zhang), weibc@imech.ac.cn (B. Wei).

https://doi.org/10.1016/j.tws.2023.110836
Received 6 February 2023; Received in revised form 3 May 2023; Accepted 5 May 2023
Available online 7 June 2023

Nomenclature

A	Area of cross-section of beam section
b	Width of beam
E	Young's modulus
$F_1(x)$, $F_2(x)$	Shifting functions for beam sections ① and ②
f^{σ}_{crit}, f^{τ}_{crit}	Acceptable dynamic factors for normal and shear stresses
f^{σ}_{dyn}, f^{τ}_{dyn}	Dynamic factors for normal and shear stresses
h	Thickness of beam
I	Second moment of area of beam section
L_0	Half of beam length
L	Half of span between two supports
$T_i(t)$, $\dot{T}_i(t)$	Modal displacement and velocity of ith normal mode
t	Time
v	Loading rate
$V(x,t)$	Shear force
$w_1(x,t)$, $w_2(x,t)$	Deflections of beam sections ① and ②
$w_{1\text{fv}}(x,t)$, $w_{2\text{fv}}(x,t)$	Free-vibration components of beam sections ① and ②
$W_{1i}(x)$, $W_{2i}(x)$	ith normal modes of beam sections ① and ②
β_i	ith mode wavenumber
γ	Ratio of beam length outside support to half span
λ_i	ith mode eigenvalue
ξ	Characteristic time
ξ_{crit}	Quasi-static time threshold
ρ	Density
σ	Dynamic normal (flexural) stress
σ_{vib}	Normal stress component due to structural vibration
σ_{sta}	Normal stress component due to quasi-static motion
τ	Dynamic shear stress
τ_{vib}	Shear stress component due to structural vibration
τ_{sta}	Shear stress component due to quasi-static motion
$\phi_{1i}(x)$, $\phi_{2i}(x)$	ith mode shapes of beam sections ① and ②
$\psi(x,t)$	Normal-to-shear stress ratio
ω_i	Angular frequency of ith vibration mode

Abbreviations

CFRPs	Carbon-fiber-reinforced plastics
DIC	Digital image correlation
FEM	Finite-element method
SHB	Split Hopkinson bar
SHM	Structural health monitoring

is related to the applied velocity, and, under low-velocity impact, the structural response is dominated by propagation of a flexural wave (providing a global dynamic response) rather than a dilatational one [37]. For specimens with finite lengths, propagation of flexural waves induces the structural vibration, giving rise to the oscillatory dynamic response of the specimen and, therefore, oscillatory applied loads. If specimens have an infinite length or can be considered long, the dominant mechanism is flexural-wave propagation without structural vibration, and readers are referred to [38].

There remain questions concerning dynamic three-point bending of finite-length specimens that have not yet been fully answered in the literature, such as the effect of specimen geometry on the dynamic response, the classification between quasi-static and dynamic loading rates, and evolution of dynamic responses, to name a few. These can be addressed with analytical investigation, and it is one of the main focuses of this work. Note that for drop-weight three-point bending tests, both the mass and initial velocity of the striker (or impact energy) affect the dynamic response of the impacted specimen. For a fundamental understanding of the intrinsic dynamic effect in the specimens, only the impact velocity is considered, that is, high loading rates, which could be achieved with SHB impact experiments.

In this work, the analytical theory of dynamic three-point bending tests under high-loading rates is developed first in Section 2 to study the dynamic effects and their evolution in association with configuration geometry, by investigating the dynamic normal (flexural) and shear stresses. The analytical solutions are then verified in Section 3 experimentally and numerically. For the experimental validation in Section 3.1, digital image correlation (DIC) results from specimens under SHB impact are used. Further verification against the finite-element-method (FEM) simulations follows in Section 3.2. Conclusions are given in Section 4. Note that although this study is focused on the rectangular cross-sectioned beams, the developed analytical techniques can be readily transferred to study other beams with various cross sections and flexural rigidities, widely investigated in the field of thin-walled structures, such as solid square cross-sectioned beams [39], cylindrical tubes [40,41], rectangular tubes [42,43], sandwich beams [44,45], channeled sectioned beams [46,47], smooth-shell lattice-filled cross-sectioned beams [48], to name a few.

2. Theory

In this section, the theory of dynamic three-point bending is developed. The dynamic normal (flexural) and shear stresses under high loading rates are derived analytically with consideration of structural vibration by employing beam dynamics. The dynamic response behavior is also investigated.

The considered beam configuration (Fig. 1a) has a total length of $(L_1 + L_2)$, a thickness of h, and a span of $2L$, with the high-loading-rate displacement acting at the midspan location. Note that in the quasi-static testing configuration, $L_1 = L_2$ is not a requirement; only that the external displacement or load is applied at the midspan, that is, loading configuration is symmetric. This, however, is not the case in the dynamic regime since the difference between L_1 and L_2 alters the normal mode (or mode shape), causing asymmetric loading (an example of this is given in Appendix A, see Fig. A.1). For symmetrical loading, $L_1 = L_2$ and so, to facilitate the derivation, a dimensionless length ratio $\gamma = (L_0 - L)/L$ is introduced, with $L_0 = L_1 = L_2$. Therefore, due to the problem's symmetry, only one half of the three-point bending configuration with two beam sections is modeled analytically, as shown in Fig. 1b, together with the prescribed coordinate system and applied displacement $w_0(t)$. The lengths of beam sections ① and ② are, then, L and γL, and their deflections are denoted $w_1(x,t)$ and $w_2(x,t)$, respectively. Assuming the beam is thin ($L \gg h$ and $\gamma L \gg h$), Euler–Bernoulli classical beam theory applies. The applied displacement is $w_0(t) = vt$, representing a high-loading-rate scenario, with v being the constant loading rate.

Theoretical investigation is arranged as follows: the deflections of the half three-point bending configuration in Fig. 1b is derived in Section 2.1, which are then used to derive the dynamic normal (flexural) and shear stresses in Section 2.2 and Section 2.3 with further investigation of dynamic effects. In Section 2.4, the potential dynamic failure modes are studied for brittle materials.

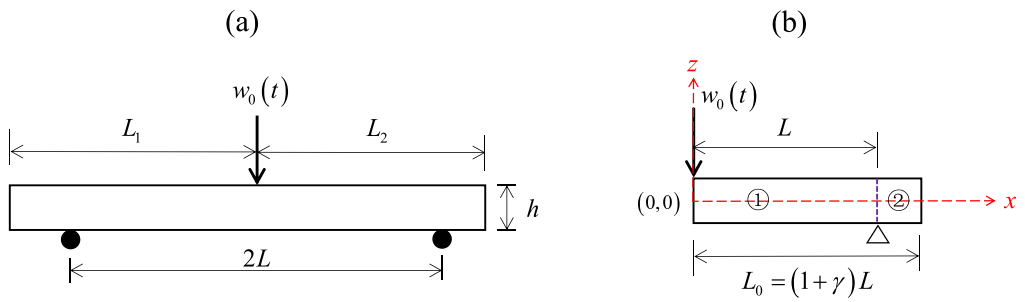

Fig. 1. (a) Schematic of three-point bending configuration; (b) analytical model with coordinate system.

2.1. Dynamic transverse response under high loading rate

2.1.1. Deflection assumptions and boundary conditions

Due to the symmetric configuration, the boundary conditions for beam section ① in Fig. 1b are $w_1^{(1)}(0,t)=0$ and $w_1(0,t)=vt$ at the loading point, and $w_1(L,t)=0$ at the support point. The boundary conditions for the beam section ② are $w_2(L,t)=0$ at the support and $EIw_2^{(2)}(L_0,t)=0$ and $EIw_2^{(3)}(L_0,t)=0$ at its free end. The equations of motion for the two beam sections are

$$EIw_1^{(4)}(x,t)+\rho A\ddot{w}_1(x,t)=0, \tag{1}$$

$$EIw_2^{(4)}(x,t)+\rho A\ddot{w}_2(x,t)=0, \tag{2}$$

where $I=bh^3/12$ is the second moment of area and $A=bh$ is the cross-sectional area. Eqs. (1) and (2) are for plane-stress conditions; for plane-strain conditions, E must be replaced with $E/(1-\nu^2)$ throughout this paper. Lagrange's notation $w^{(1)}=\partial w/\partial x$ is used to represent partial differentiation with respect to the x coordinate, and the 'over dot' notation $\dot{w}=\partial w/\partial t$ is used for the partial differentiation with respect to time.

Under high loading rates, the dynamic response of the beam includes a free vibration and a quasi-static motion, and the total deflections $w_1(x,t)$ and $w_2(x,t)$ can be expressed as combinations of the free-vibration component and extrapolation of the applied displacements as the quasi-static component by introducing the shifting functions, giving

$$w_1(x,t)=w_{1\mathrm{fv}}(x,t)+F_1(x)vt, \tag{3}$$

$$w_2(x,t)=w_{2\mathrm{fv}}(x,t)+F_2(x)vt, \tag{4}$$

where $w_{1\mathrm{fv}}(x,t)$ and $w_{2\mathrm{fv}}(x,t)$ are the free-vibration components of beam sections ① and ②, respectively; $F_1(x)$ and $F_2(x)$ are the corresponding shifting functions used to distribute the applied displacement along the beam lengths. Combining Eqs. (1) and (3) and applying the homogeneity condition, the governing equations for the free-vibration component and the shifting function for the beam section ① are obtained as

$$EIw_{1\mathrm{fv}}^{(4)}(x,t)+\rho A\ddot{w}_{1\mathrm{fv}}(x,t)=0, \tag{5}$$

$$F_1(x)=0. \tag{6}$$

Similarly, for the beam section ②, by combining Eqs. (2) and (4), the respective governing equations are

$$EIw_{2\mathrm{fv}}^{(4)}(x,t)+\rho A\ddot{w}_{2\mathrm{fv}}(x,t)=0, \tag{7}$$

$$F_2(x)=0. \tag{8}$$

The boundary conditions for the free-vibration components $w_{1\mathrm{fv}}(x,t)$ and $w_{2\mathrm{fv}}(x,t)$ and the shifting functions $F_1(x)$ and $F_2(x)$ are given in Appendix B along with the continuity conditions.

2.1.2. Solution for shifting functions

By solving the governing equations Eqs. (6) and (8) with the boundary conditions in Table B.1 and Table B.2, the shifting functions are obtained as

$$F_1(x)=\frac{1}{2L^3}x^3-\frac{3}{2L^2}x^2+1, \tag{9}$$

$$F_2(x)=-\frac{3}{2L}x+\frac{3}{2}. \tag{10}$$

It is worth noting that the shifting function $F_1(x)$, represents the displacement extrapolation $vtF_1(x)$, and the velocity distribution $vF_1(x)$ as the quasi-static component, is independent of γ, that is, the length of the beam section ② does not affect the quasi-static response. Therefore, in a quasi-static three-point bending test, the lengths outside the supports, or "overhang", are not of concern, but, as demonstrated later in this work, this is not the case for dynamic regime.

2.1.3. Solution for free-vibration components

The general solutions for Eqs. (5) and (7), with the method of separation of variables, are

$$w_{1\mathrm{fv}}(x,t)=\sum_{i=1}^{\infty}W_{1i}(x)T_i(t), \tag{11}$$

$$w_{2\mathrm{fv}}(x,t)=\sum_{i=1}^{\infty}W_{2i}(x)T_i(t), \tag{12}$$

where $W_{1i}(x)$ and $W_{2i}(x)$ are the ith normal modes of beam sections ① and ②, respectively; and $T_i(t)$ is the ith modal displacement. Combining Eqs. (5) and (11), Eqs. (7) and (12), and introducing natural frequency ω_i, two ordinary governing equations for normal modes and one equation for a modal displacement are derived:

$$W_{1i}^{(4)}(x)-\beta_i^4W_{1i}(x)=0, \tag{13}$$

$$W_{2i}^{(4)}(x)-\beta_i^4W_{2i}(x)=0, \tag{14}$$

$$\ddot{T}_i(t)+\omega_i^2T_i(t)=0, \tag{15}$$

where β_i is the wavenumber with $\beta_i^4=\omega_i^2\rho A/(EI)$.

The solution for the normal mode $W_{1i}(x)$ of beam section ① can be obtained by solving Eq. (13) together with the boundary conditions given in Table B.1 as

$$W_{1i}(x)=C_{i1}\phi_{1i}(x), \tag{16}$$

where C_{i1} is the coefficient to be determined and $\phi_{1i}(x)$ is the mode shape,

$$\phi_{1i}(x)=\cosh(\beta_ix)-\cos(\beta_ix)-\frac{[\cosh(\lambda_i)-\cos(\lambda_i)]}{[\sinh(\lambda_i)-\sin(\lambda_i)]}[\sinh(\beta_ix)-\sin(\beta_ix)], \tag{17}$$

with $\lambda_i=\beta_iL$ being the eigenvalue, which can be obtained by solving the frequency equation in Eq. (20).

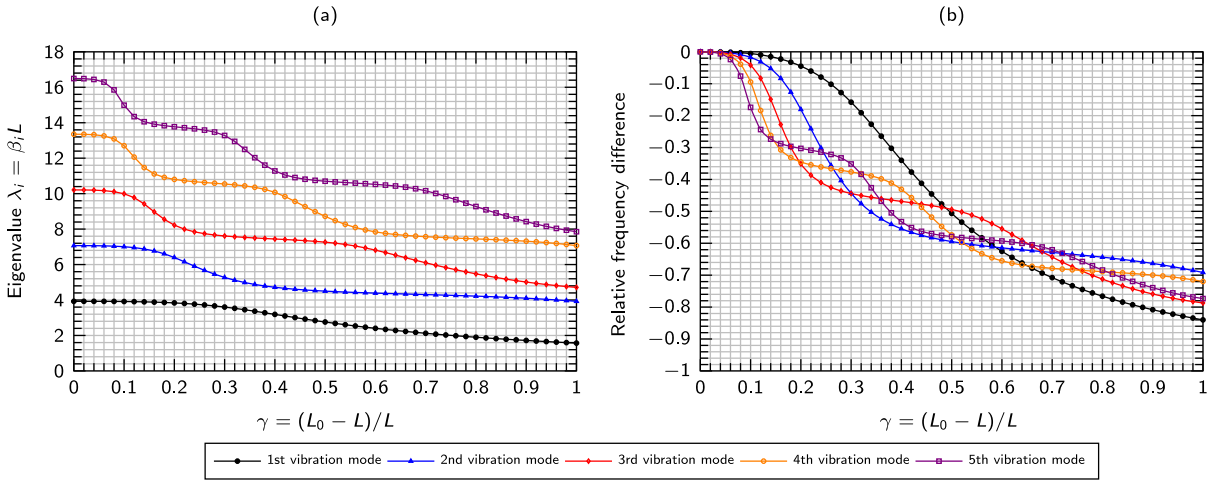

Fig. 2. (a) Eigenvalues as function of beam length ratio γ; (b) effect of beam length ratio γ on relative natural frequency difference.

The solution for normal mode $W_{2i}(x)$ of beam section ② can be obtained by solving Eq. (7) together with the boundary conditions given in Table B.2 and continuity conditions in Table B.3 as

$$W_{2i}(x) = C_{i1}\phi_{2i}(x)\,, \tag{18}$$

where the mode shape $\phi_{2i}(x)$ is

$$\begin{aligned}\phi_{2i}(x) = &\frac{[\cos(\lambda_i)\cosh(\lambda_i)-1]}{[\sinh(\lambda_i)-\sin(\lambda_i)]}\frac{[\sinh(\gamma\lambda_i)+\sin(\gamma\lambda_i)]}{[\cos(\gamma\lambda_i)\cosh(\gamma\lambda_i)+1]}\left\{\cosh\left[\beta_i(x-L_0)\right]+\cos\left[\beta_i(x-L_0)\right]\right\}\\ &+\frac{[\cos(\lambda_i)\cosh(\lambda_i)-1]}{[\sinh(\lambda_i)-\sin(\lambda_i)]}\frac{[\cosh(\gamma\lambda_i)+\cos(\gamma\lambda_i)]}{[\cos(\gamma\lambda_i)\cosh(\gamma\lambda_i)+1]}\left\{\sinh\left[\beta_i(x-L_0)\right]+\sin\left[\beta_i(x-L_0)\right]\right\}.\end{aligned} \tag{19}$$

Applying the continuity conditions to the normal modes gives the frequency equation as

$$\begin{aligned}&\left[\cos(\lambda_i)\cosh(\lambda_i)-1\right]\left[\cos(\gamma\lambda_i)\sinh(\gamma\lambda_i)-\cosh(\gamma\lambda_i)\sin(\gamma\lambda_i)\right]\\ &+\left[\cos(\gamma\lambda_i)\cosh(\gamma\lambda_i)+1\right]\left[\cos(\lambda_i)\sinh(\lambda_i)-\cosh(\lambda_i)\sin(\lambda_i)\right]=0.\end{aligned} \tag{20}$$

The eigenvalues in Eq. (20) are a function of the beam length ratio γ, which depends on the specimen configuration. The eigenvalues of the first five vibration modes for beam length ratios in the range $(0,1)$ are shown in Fig. 2a. Also, the relationship between the eigenvalues and the natural frequencies is $\omega_i = (\lambda_i^2/L^2)\sqrt{EI/(\rho A)}$, and, therefore, the value of γ also influences the natural frequencies. This can be seen in Fig. 2b, where a relative frequency difference $\Delta\omega_i = [\omega_i(\gamma) - \omega_i(\gamma=0)]/\omega_i(\gamma=0)$ is introduced based on a baseline of $\gamma = 0$. It is seen that the effect of the beam length ratio γ on the natural frequencies is significant and the design of specimen configuration must take this into account. It should be also noted that ASTM 7264 [29] recommends $\gamma = 0.2$, and, in this case, the eigenvalues λ_i for the first five vibration modes are 3.83757, 6.39890, 8.22396, 10.80461 and 13.77274, respectively.

Now, C_{i1} is the only coefficient left undetermined for the normal modes $W_{1i}(x)$ in Eq. (16) and $W_{2i}(x)$ in Eq. (18). It can be obtained by employing the orthogonality condition in Eq. (C.5), which is derived in Appendix C, resulting in

$$C_{i1}^2 = \frac{EI}{\rho A}\frac{1}{\left\{\int_0^L\left[\phi_{1i}(x)\right]^2dx+\int_L^{L_0}\left[\phi_{2i}(x)\right]^2dx\right\}}. \tag{21}$$

The general form for the solution of modal displacement is

$$T_i(t) = T_i(0)\cos(\omega_i t) + \frac{\dot{T}_i(0)}{\omega_i}\sin(\omega_i t)\,, \tag{22}$$

where $T_i(0)$ and $\dot{T}_i(0)$ are the initial modal displacement and velocity, respectively, derived in Appendix D as

$$T_i(0) = \frac{\rho A}{EI}\left[\int_0^L W_{1i}(x)\,w_{1\mathrm{fv}}(x,0)\,dx+\int_L^{L_0}W_{2i}(x)\,w_{2\mathrm{fv}}(x,0)\,dx\right], \tag{23}$$

$$\dot{T}_i(0) = \frac{\rho A}{EI}\left[\int_0^L W_{1i}(x)\,\dot{w}_{1\mathrm{fv}}(x,0)\,dx+\int_L^{L_0}W_{2i}(x)\,\dot{w}_{2\mathrm{fv}}(x,0)\,dx\right]. \tag{24}$$

Note that $w_{1\mathrm{fv}}(0,t)$ and $w_{2\mathrm{fv}}(0,t)$ can be obtained by setting $t=0$ in Eqs. (3) and (4), giving $w_{1\mathrm{fv}}(0,t)=0$ and $w_{2\mathrm{fv}}(0,t)=0$; and similarly, $\dot{w}_{1\mathrm{fv}}(0,t) = -vF_1(x)$ and $\dot{w}_{2\mathrm{fv}}(0,t) = -vF_2(x)$. And then from Eq. (23), the initial modal displacement $T_i(0)=0$; and, from Eq. (24), the initial modal velocity, derived in Appendix E, is

$$\dot{T}_i(0) = v\frac{1}{\omega_i^2}W_{1i}^{(3)}(0)\,. \tag{25}$$

Therefore, by combining results in Sections 2.1.2 and 2.1.3, the total deflection for beam section ① is

$$w_1(x,t) = -2vL^2\sqrt{\frac{\rho A}{EI}}\sum_{i=1}^{\infty}\frac{H_i}{\lambda_i^3}\phi_i(x)\sin(\omega_i t)+\left(\frac{1}{2L^3}x^3-\frac{3}{2L^2}x^2+1\right)vt\,, \tag{26}$$

where

$$H_i = \frac{\left[\cosh(\lambda_i)-\cos(\lambda_i)\right]}{\left[\sinh(\lambda_i)-\sin(\lambda_i)\right]}\frac{L}{\left\{\int_0^L\left[\phi_{1i}(x)\right]^2dx+\int_L^{L_0}\left[\phi_{2i}(x)\right]^2dx\right\}}. \tag{27}$$

Note that only the deflection of beam section ① is considered since damage and failure can initiate in this region.

2.2. Dynamic normal stress

The normal (flexural) stress across the beam section, according to beam mechanics, is $\sigma(x,z,t) = -M(x,t)\,z/I$ with $M(x,t)$ being the internal bending moment. By using the deflection of beam section ① in Eq. (26), the total dynamic normal (flexural) stress is obtained as

$$\sigma(x,z,t) = 4\sqrt{3}v\sqrt{\rho E}\frac{z}{h}\sum_{i=1}^{\infty}\mathrm{X}_i(x,\gamma)\sin(\omega_i t)+\left(1-\frac{1}{L}x\right)\frac{z}{h}\frac{3Ehvt}{L^2}, \tag{28}$$

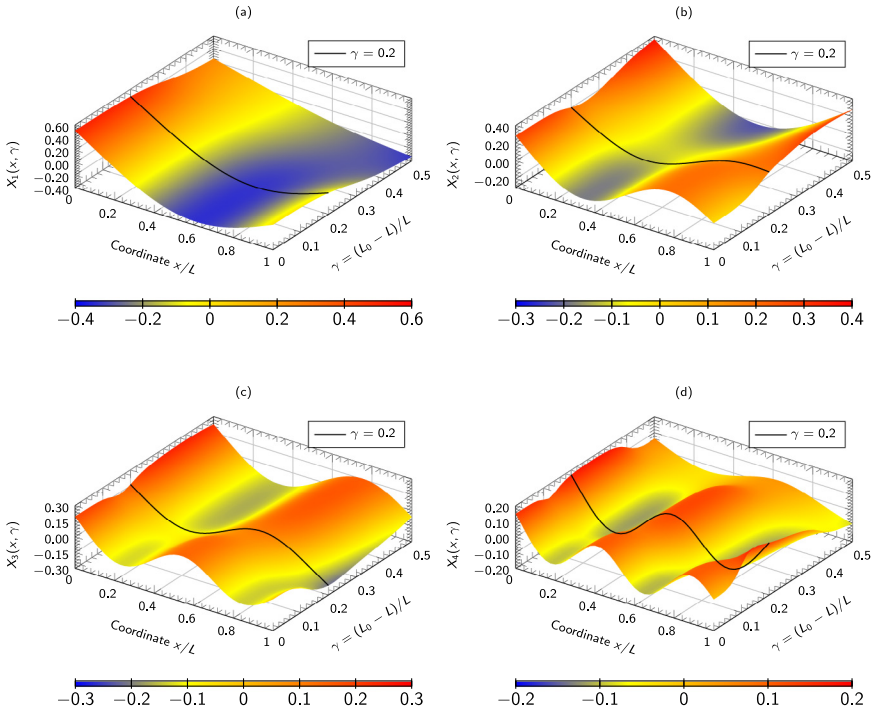

Fig. 3. Contribution of first four vibration modes to dynamic normal stress for $0 \le \gamma \le 0.5$: (a) first mode, (b) second mode, (c) third and (d) fourth mode.

where

$$\mathrm{X}_i(x,\gamma) = \frac{H_i}{\lambda_i}\left\{\left[\cosh\left(\frac{\lambda_i}{L}x\right)+\cos\left(\frac{\lambda_i}{L}x\right)\right] - \frac{\left[\cosh(\lambda_i)-\cos(\lambda_i)\right]}{\left[\sinh(\lambda_i)-\sin(\lambda_i)\right]}\left[\sinh\left(\frac{\lambda_i}{L}x\right)+\sin\left(\frac{\lambda_i}{L}x\right)\right]\right\}. \quad (29)$$

The normal (flexural) stress in Eq. (28) consists of two components – related to the structural vibration and the quasi-static motion – denoted σ_{vib} and σ_{sta}, respectively. The latter is a function of coordinates (x, z), and it reaches its maximum value at the loading point $(x = 0)$, vanishing at the support $(x = L)$. The flexural-stress component due to structural vibration (or vibration-induced normal stress) σ_{vib} is a function of coordinate x and the beam length ratio γ via $\mathrm{X}_i(x,\gamma)$, which is investigated in Section 2.2.1.

2.2.1. Contribution of ith vibration mode to dynamic flexural stress

Eq. (28) shows that the contribution to the vibration-induced normal stress component σ_{vib} from the ith vibration mode is proportional to $\mathrm{X}_i(x,\gamma)$ that depends on the ratio γ of the beam length outside $(L_0 - L)$ support to the half span L (i.e. $\gamma = (L_0 - L)/L$). The distributions of values of $\mathrm{X}_i(x,\gamma)$ for the first four vibration modes along the span for $0 \le \gamma \le 0.5$ are plotted in Fig. 3 together with their magnitudes.

As seen in Fig. 3, the contribution of each vibration is oscillatory with regard to both the coordinate x and the beam length ratio γ, with a rather complex trend. Since in ASTM 7264 [29] it is recommended that $\gamma = 0.2$, $\mathrm{X}_i(x, 0.2)$ as the cross-section of Fig. 3 is presented in Fig. 4 together with its absolute values.

It is clear that $\mathrm{X}_i(x, 0.2)$ oscillates around zero. For the ith vibration mode there are i roots for $\mathrm{X}_i(x, 0.2) = 0$, for which the mode does not contribute to the vibration-induced normal stress component σ_{vib}. This can be used by researchers in the field of structural health monitoring (SHM) for acquiring stress signals free of a certain vibration frequency. In addition, at the loading point $(x = 0)$, with the maximum normal stress, the first vibration mode makes the greatest contribution with $\mathrm{X}_1(0, 0.2) = 0.4863$, but the dominant vibration mode alters along the span (coordinate x). Based on the absolute value of $\mathrm{X}_i(x, 0.2)$, the beam section can be divided into three regions according to the dominant vibration mode (Fig. 4b): (1) Region I with $0 \le x \le 0.205L$; (2) Region II with $0.205L \le x \le 0.355L$; (3) Region III with $0.355L \le x \le L$. The first vibration mode dominates in Regions I and III, while other vibration modes dominate in Region II.

2.2.2. Normal-stress dynamic factor and strain rate

To study the dynamic effect, a normal-stress dynamic factor $f^{\sigma}_{\mathrm{dyn}}(x,\gamma,t)$ is defined as the ratio between the normal stress components due to vibration and quasi-static motion, that is,

$$f^{\sigma}_{\mathrm{dyn}}(x,\gamma,t) = \frac{\sigma_{\mathrm{vib}}}{\sigma_{\mathrm{sta}}} = \frac{4\sqrt{3}v\sqrt{\rho E}\frac{z}{h}\sum_{i=1}^{\infty}\mathrm{X}_i(x,\gamma)\sin(\omega_i t)}{\left(1-\frac{1}{L}x\right)\frac{z}{h}\frac{3Ehvt}{L^2}} = \frac{2}{3}\frac{L^2}{t}\sqrt{\frac{\rho A}{EI}}\frac{1}{\left(1-\frac{1}{L}x\right)}\sum_{i=1}^{\infty}\mathrm{X}_i(x,\gamma)\sin\left(\frac{\lambda_i^2}{L^2}\sqrt{\frac{EI}{\rho A}}t\right). \quad (30)$$

Note that this dynamic factor is independent of coordinate z but a function of coordinate x and time t. Its properties can be further studied by defining a characteristic time,

$$\xi = \frac{1}{L^2}\sqrt{\frac{EI}{\rho A}}t, \quad (31)$$

that is an intrinsic property of the investigated configuration. By substituting Eq. (31) into Eq. (30), the dynamic factor for normal stress can be expressed by the characteristic time as

$$f^{\sigma}_{\mathrm{dyn}}(x,\gamma,\xi) = \frac{2}{3}\frac{1}{\xi}\frac{1}{(1-x/L)}\sum_{i=1}^{\infty}\mathrm{X}_i(x,\gamma)\sin\left(\lambda_i^2\xi\right). \quad (32)$$

The evolution of this dynamic factor with the characteristic time for $\gamma = 0.2$ is presented in Fig. 5 for the first ten vibration modes.

The factor oscillates around zero, decreasing with respect to the characteristic time, and its absolute magnitude drops below 0.1 after $\xi = 3.25$. In a real-life experiments, the characteristic time is associated with the failure of the material, and by relating the characteristic time

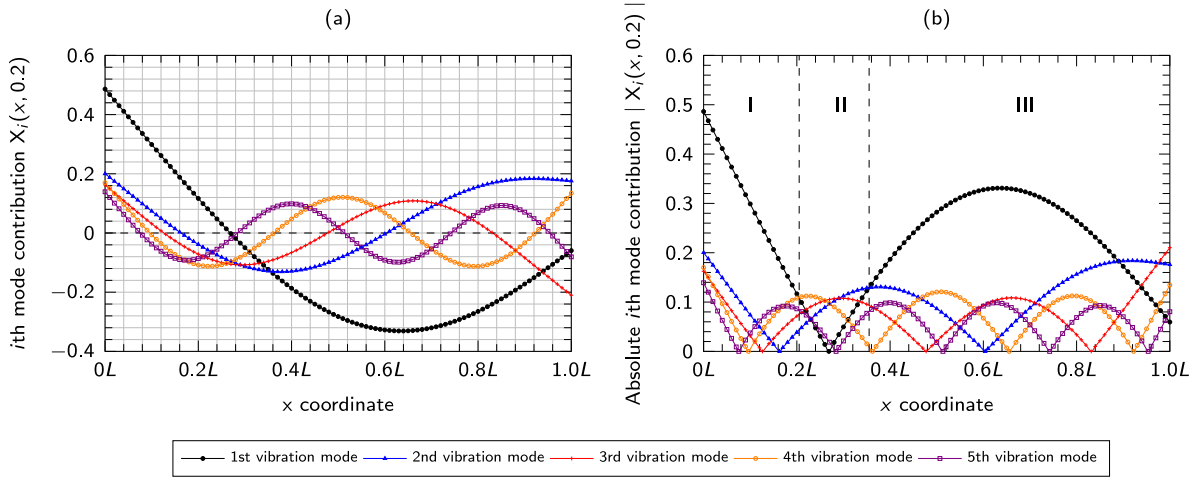

Fig. 4. Contribution of ith vibration mode to dynamic normal stress for $\gamma = 0.2$ (a) and its absolute value (b) for various x.

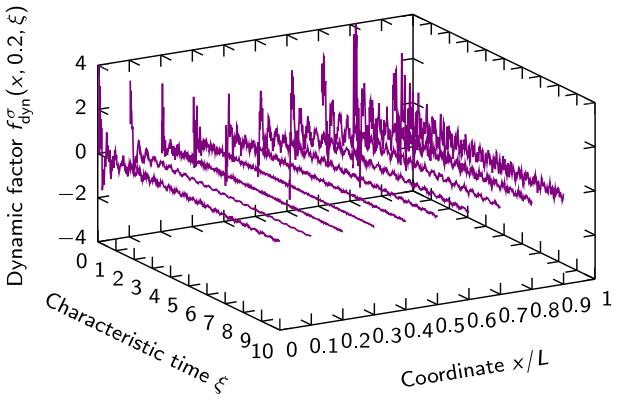

Fig. 5. Evolution of normal-stress dynamic factor with characteristic time for $\gamma = 0.2$ for first ten vibration modes.

back to the testing time for failure via Eq. (31), the respective dynamic factor can be determined as an indicator of dynamic effect.

Another parameter usually employed to study the dynamic effect is the strain rate, which can be derived by Eq. (28), giving

$$\dot{\varepsilon}_{xx}(x,z,t) = \frac{d\varepsilon_{xx}(x,z,t)}{dt} = \frac{1}{E}\frac{d\sigma(x,z,t)}{dt} = 4\sqrt{3}v\sqrt{\frac{\rho}{E}}\frac{z}{h}\sum_{i=1}^{\infty}\omega_i \mathrm{X}_i(x,\gamma)\cos(\omega_i t) + \left(1-\frac{1}{L}x\right)\frac{z}{h}\frac{3hv}{L^2}. \tag{33}$$

The strain rate is also comprised of two components: the vibration-induced strain rate and the quasi-static-motion strain rate. In the former, the higher vibration modes make higher contributions thanks to the multiplier of the natural frequency ω_i. The quasi-static-motion strain rate is only a function of coordinates (x, z), and once the location is fixed, this motion gives a fixed strain-rate contribution, proportional to the loading rate v. An example can be seen for the coordinates $(0, -h/2)$ the bottom side under the loading point of the beam, with the maximum normal (tensile) stress, where the strain rate is

$$\dot{\varepsilon}_{xx}\left(0,-\frac{h}{2},t\right) = -2\sqrt{3}v\sqrt{\frac{\rho}{E}}\sum_{i=1}^{\infty}\omega_i \mathrm{X}_i(0,\gamma)\cos(\omega_i t) - \frac{3hv}{2L^2}. \tag{34}$$

By incorporating the characteristic time ξ defined in Eq. (31), this strain rate is

$$\dot{\varepsilon}_{xx}\left(0,-\frac{h}{2},\xi\right) = -v\frac{h}{L^2}\left[\sum_{i=1}^{\infty}\lambda_i^2 \mathrm{X}_i(0,\gamma)\cos\left(\lambda_i^2\xi\right) + \frac{3}{2}\right]. \tag{35}$$

The evolution of the total strain rate for characteristic time $0 \le \xi \le 5$ and $\gamma = 0.2$ is shown in Fig. 6a for the first vibration mode and in Fig. 6b for the first ten vibration in comparison with the quasi-static strain rate. The total strain rate oscillates with higher vibration modes contributing more to the total strain rate. Hence, the oscillatory nature of the strain rate for dynamic three-point configuration makes it not suitable as a quantitative measure of the dynamic effect.

2.2.3. Quasi-static time threshold and loading condition

The three-point bending configuration under high loading rate undergoes structural vibration and gives rise to a significant dynamic effect as the previous section shows. This raises an important question about the value of loading rate associated with the evolution of dynamic factor, above which the case can be considered dynamic, and below which quasi-static.

The analysis in Section 2.2.2 demonstrates that the dynamic factor for normal stress $f^{\sigma}_{\mathrm{dyn}}(x, 0.2, \xi)$ attenuates with respect to the characteristic time ξ, becoming negligibly small after a certain characteristic time ξ. This indicates that there exist both a time threshold ξ_{crit}, above which the dynamic effect can be safely ignored, and a corresponding quasi-static loading rate. Considering the maximum normal stress at $(0, -h/2)$, the time evolution of the dynamic factor for normal stress by substituting $x = 0$ into Eq. (32) is

$$f^{\sigma}_{\mathrm{dyn}}(0, 0.2, \xi) = \frac{2}{3}\frac{1}{\xi}\sum_{i=1}^{\infty}\mathrm{X}_i(0, 0.2)\sin\left(\lambda_i^2\xi\right). \tag{36}$$

To determine the time threshold ξ_{crit} beyond which the dynamic factor $\left|f^{\sigma}_{\mathrm{dyn}}(0, 0.2, \xi)\right|$ is within an acceptable value of $f^{\sigma}_{\mathrm{crit}}$, the envelope (the red dashed line in Fig. 7a) of $f^{\sigma}_{\mathrm{dyn}}(0, 0.2, \xi)$ can be employed. Then, the relation between the acceptable value of dynamic factor $f^{\sigma}_{\mathrm{crit}}$ and the corresponding time threshold ξ_{crit} can be plotted with its quantitative regression in Fig. 7b.

It is seen that the acceptable dynamic factor varies log-linearly with the time threshold ξ_{crit} (Fig. 7b). For $\xi > \xi_{\mathrm{crit}} = 81.41$, the acceptable value of dynamic factor is less than 0.01 meaning that the dynamic effect accounts for less than 1% of the normal stress.

Now consider the quasi-static loading condition, that is, normal failure happens quasi-statically below a certain maximum loading rate. Assuming the material's normal (flexural) strength σ_{crit} is rate-independent, combining Eqs. (28) and (30), the failure criterion is then

$$\sigma\left(0,-\frac{h}{2},t\right) = -\left[1 + f^{\sigma}_{\mathrm{dyn}}(0, 0.2, t)\right]\frac{3Ehvt}{2L^2} = \sigma_{\mathrm{crit}}. \tag{37}$$

By incorporating the definition of characteristic time ξ in Eq. (31) and the concept of an acceptable value of the dynamic factor $f^{\sigma}_{\mathrm{crit}}$ with the associated time threshold ξ_{crit}, the following loading-rate condition

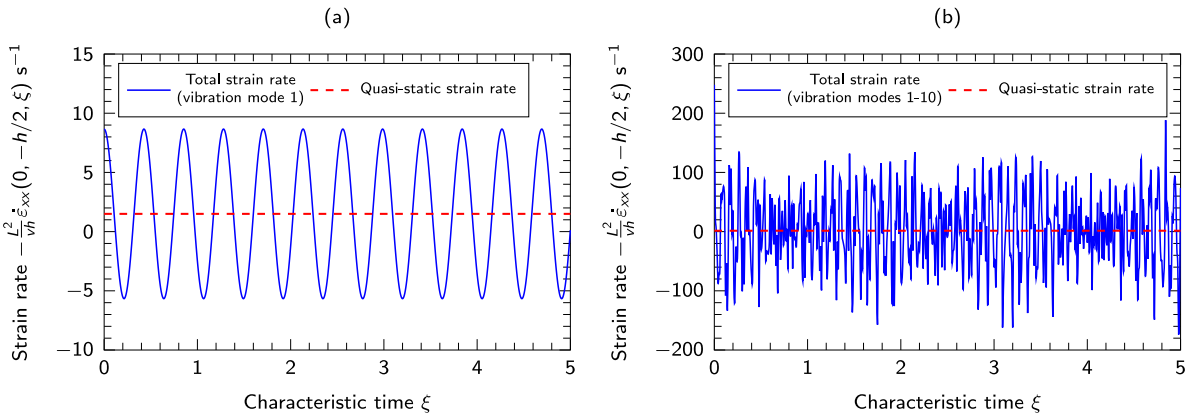

Fig. 6. Total strain rate with first (a) and first ten vibration (b) modes.

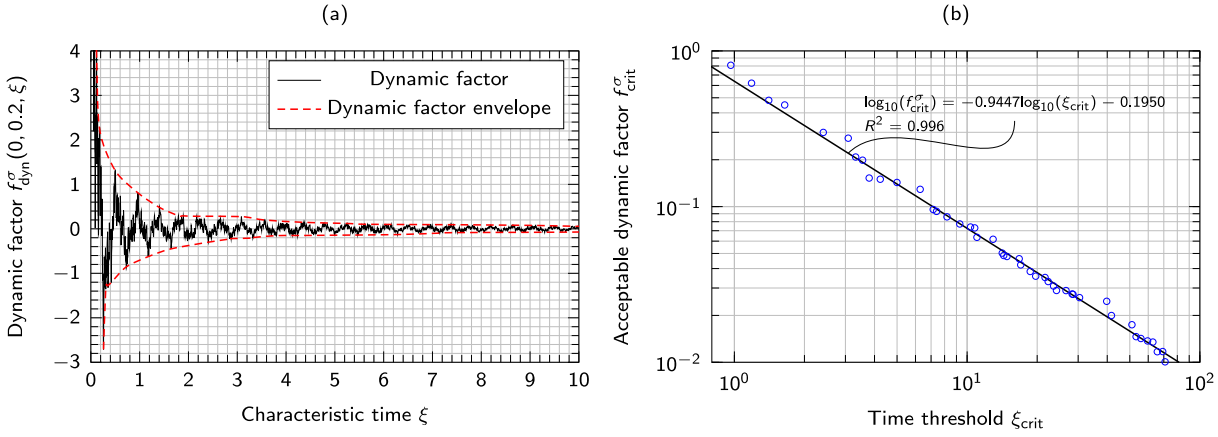

Fig. 7. (a) Dynamic factor for normal stress and its envelope; (b) relation between acceptable normal-stress dynamic factor and characteristic time threshold.

based on Eq. (37) must be satisfied:

$$|v| \le \frac{\sqrt{3}}{9}\frac{1}{\xi_{\text{crit}}\left(1+f^{\sigma}_{\text{crit}}\right)}\frac{\sigma_{\text{crit}}}{\sqrt{E\rho}}. \tag{38}$$

Employing the result in Fig. 7b for the relation between the acceptable value of dynamic factor f^{σ}_{crit} and the time threshold ξ_{crit}, for the acceptable dynamic factor less than 1% with $\xi_{\text{crit}} = 81.41$, the loading rate must be

$$|v| \le 0.00234\frac{\sigma_{\text{crit}}}{\sqrt{E\rho}}. \tag{39}$$

The derivation of Eqs. (38) and (39) together with Fig. 7 defines a boundary below which a test may be considered as quasi-static and can be used as a guideline for test design. For example, considering a typical CFRP with a longitudinal modulus of 120 GPa, a density of 1250 kg m^{-3} and a flexural strength of 1.2 GPa, the maximum loading rate for the quasi-static condition with the acceptable dynamic factor of 0.01 is 0.23 m s^{-1}. This result is very useful to researchers in experimental field since it provides the upper boundary for the loading rate without a significant dynamic effect, while the material's response due to the rate effect can be isolated and studied.

2.3. Dynamic shear stress

The shear stress across the beam section is $\tau(x,z,t) = V(x,t)\left(h^2/4 - z^2\right)/(2I)$, with $V(x,t)$ being the shear force. By combining the deflection in Eq. (26), the distribution of total dynamic shear stress is

$$\tau(x,z,t) = \left[-2\sqrt{3}\frac{h}{L}v\sqrt{\rho E}\sum_{i=1}^{\infty}\Lambda_i(x,\gamma)\sin\left(\omega_i t\right) + \frac{3Eh^2vt}{2L^3}\right]\left(\frac{1}{4} - \frac{z^2}{h^2}\right), \tag{40}$$

where

$$\Lambda_i(x,\gamma) = H_i\left\{\left[\sinh\left(\beta_i x\right) - \sin\left(\beta_i x\right)\right] - \frac{\left[\cosh\left(\lambda_i\right) - \cos\left(\lambda_i\right)\right]}{\left[\sinh\left(\lambda_i\right) - \sin\left(\lambda_i\right)\right]}\left[\cosh\left(\beta_i x\right) + \cos\left(\beta_i x\right)\right]\right\}. \tag{41}$$

Like the dynamic flexural stress in Eq. (28), the shear stress also consists of two components: the first term in Eq. (40) is due to the structural vibration (or vibration-induced shear stress) and denoted τ_{vib} to facilitate the subsequent discussion; the second term is due to the applied quasi-static motion and denoted τ_{sta}. Obviously, the quasi-static component τ_{sta} does not oscillate; it increases linearly with respect to time t and has a constant value for a given coordinate z. In contrast, τ_{vib} oscillates with time and is also a function of coordinate x and the beam length ratio γ via $\Lambda_i(x,\gamma)$. As shown below, the superposition of τ_{vib} and τ_{sta} as a result of combined quasi-static motion and vibration from the dynamic effect can be significant for failure initiation.

2.3.1. Contribution of ith vibration mode to dynamic shear stress

Eqs. (40) and (41) demonstrate that the contribution to the shear stress component τ_{vib} from the ith structural vibration mode is proportional to $\Lambda_i(x,\gamma)$. The values and magnitudes of $\Lambda_i(x,\gamma)$ for the first four vibration modes along the half span of the three-point bending specimen were solved and are plotted in Fig. 8.

The contribution to the dynamic shear stress from each vibration mode varies as a function of the location and the beam length ratio γ. The $\Lambda_i(x,0.2)$ cross-section of Fig. 8 is presented in Fig. 9, which represents the beam length ratio of $\gamma = 0.2$ that is recommended by ASTM D7264 [29].

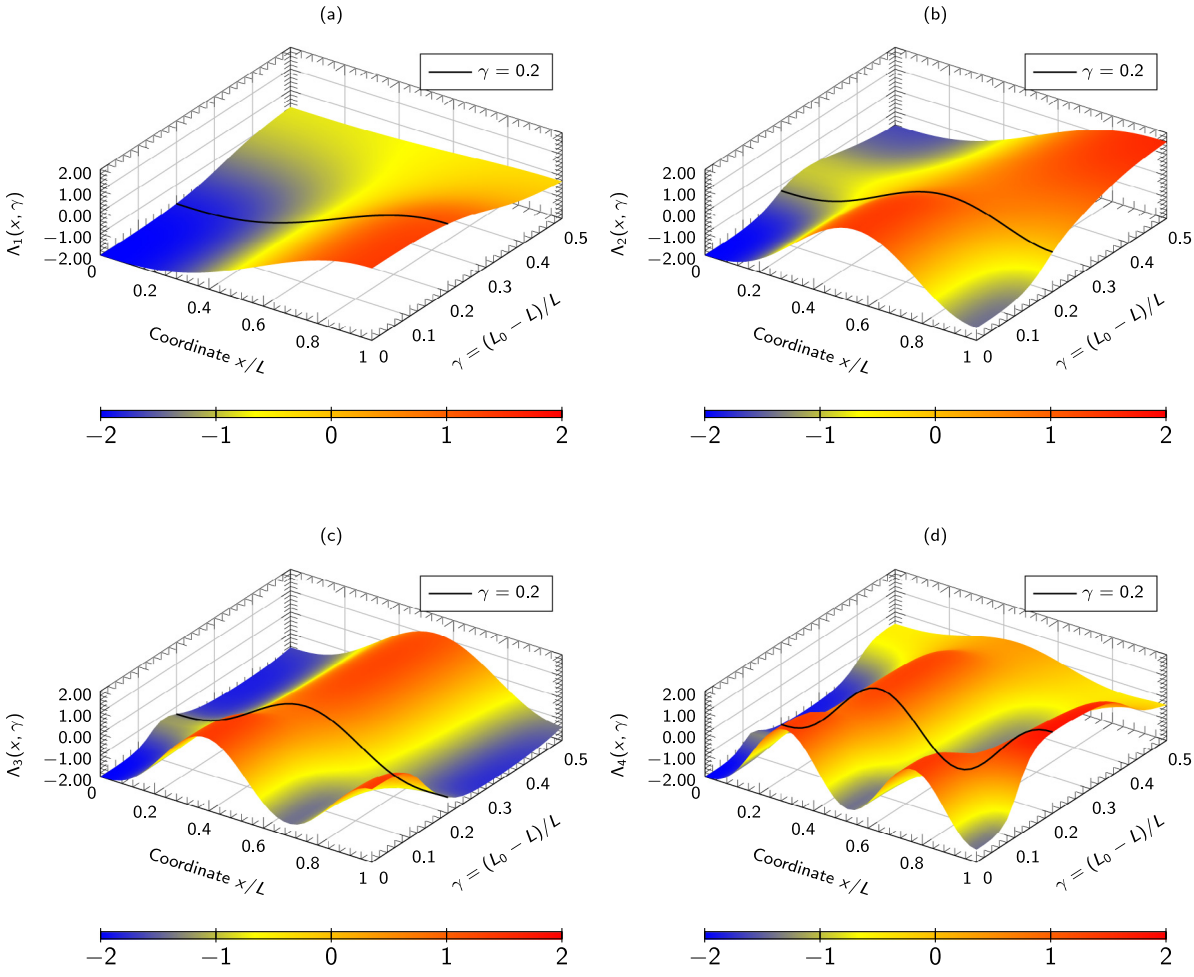

Fig. 8. Contribution of first four vibration modes to dynamic shear stress for $0 \le \gamma \le 0.5$: (a) first mode, (b) second mode, (c) third mode and (d) fourth mode.

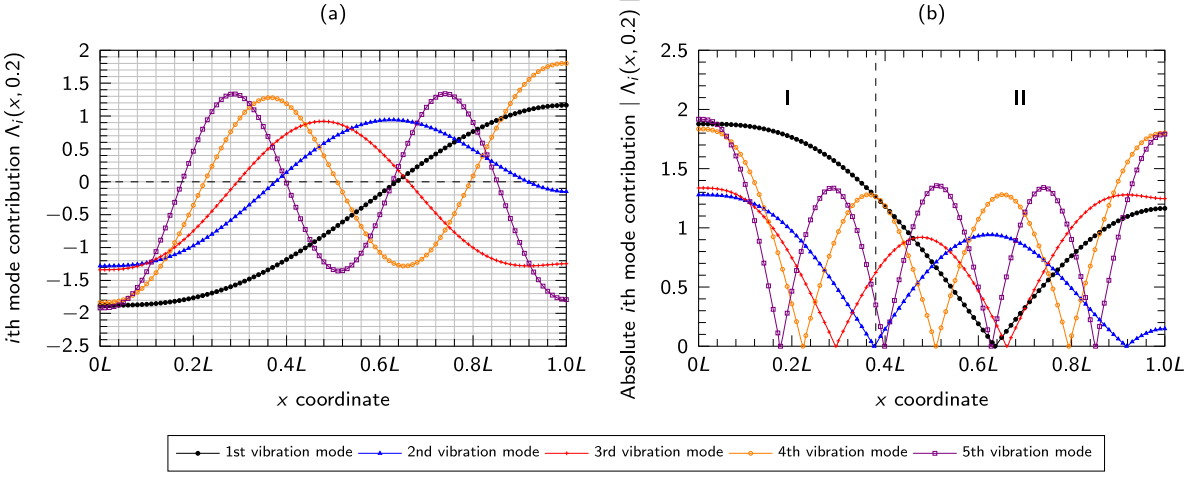

Fig. 9. Contribution of ith vibration mode to dynamic shear stress for $\gamma = 0.2$ (a) and its magnitude (b) for various x.

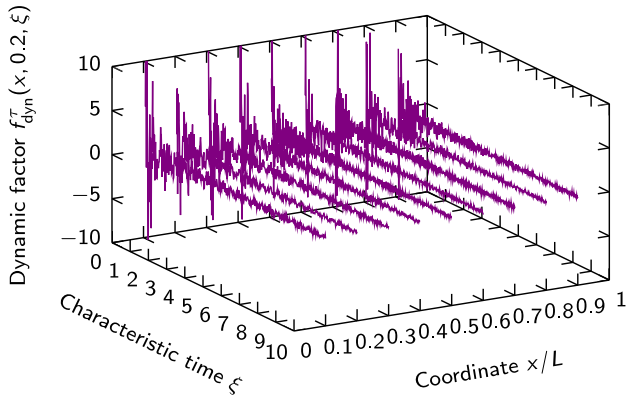

Fig. 10. Evolution of shear-stress dynamic factor with characteristic time for first ten vibration modes.

The contribution of each vibration mode varies with respect to the location (x coordinate) (Fig. 9). The half span of the beam can be approximately divided into two regions: Region I with $0 \le x \le 0.38L$ where the first vibration mode dominates and Region II where other vibration modes are significant. Also, for the ith vibration mode, there are roots of $\Lambda_i(x, 0.2) = 0$; at these points this mode does not contribute to the shear stress.

2.3.2. Shear-stress dynamic factor

To study the dynamic effect, a shear-stress dynamic factor $f^{\tau}_{\mathrm{dyn}}(x, \gamma, t)$ is defined as the ratio between the shear stress components due to vibration and quasi-static motion:

$$f^{\tau}_{\mathrm{dyn}}(x,\gamma,t) = \frac{\tau_{\mathrm{vib}}}{\tau_{\mathrm{sta}}} = \frac{\left[-2\sqrt{3}\frac{h}{L}v\sqrt{\rho E}\sum_{i=1}^{\infty}\Lambda_i(x,\gamma)\sin(\omega_i t)\right]\left(\frac{1}{4}-\frac{z^2}{h^2}\right)}{\frac{3Eh^2vt}{2L^3}\left(\frac{1}{4}-\frac{z^2}{h^2}\right)} = -\frac{2}{3}\frac{L^2}{t}\sqrt{\frac{\rho A}{EI}}\sum_{i=1}^{\infty}\Lambda_i(x,\gamma)\sin\left(\frac{\lambda_i^2}{L^2}\sqrt{\frac{EI}{\rho A}}t\right). \tag{42}$$

To investigate the evolution of this dynamic factor with respect to time, the dimensionless characteristic time in Eq. (31) is combined with the above shear stress dynamic factor, and the dynamic factor becomes

$$f^{\tau}_{\mathrm{dyn}}(x,\gamma,\xi) = -\frac{2}{3}\frac{1}{\xi}\sum_{i=1}^{\infty}\Lambda_i(x,\gamma)\sin\left(\lambda_i^2\xi\right). \tag{43}$$

The evolution of this shear-stress dynamic factor $f^{\tau}_{\mathrm{dyn}}(x,\gamma,\xi)$ for $\gamma = 0.2$ and various x coordinates with respect to the characteristic time ξ is given in Fig. 10.

Considering the combined contribution of first ten vibration modes (Fig. 10), the shear-stress dynamic factor also attenuates with characteristic time but not as quickly as the normal-stress one shown in Fig. 5.

2.3.3. Quasi-static time threshold and loading condition

Like the quasi-static time threshold for dynamic normal stress in Section 2.2.3, the quasi-static time threshold for dynamic shear stress can be obtained by examining the envelope (Fig. 11a) of the dynamic factor for shear stress at the $(0, 0)$ coordinate, considering the maximum modal contribution at $x = 0$ (Fig. 9). Following a similar approach, the relation between the acceptable value of dynamic factor f^{τ}_{crit} and the corresponding time threshold ξ_{crit} was obtained (Fig. 11b).

The acceptable dynamic factor f^{τ}_{crit} also varies log-linearly with respect to the time threshold ξ_{crit}. For $\xi > \xi_{\mathrm{crit}} = 902.72$, the acceptable value of dynamic factor is less than 0.01 meaning that the dynamic effect accounts for less than 1% of the total shear stress. Recalling the respective result for the time threshold for normal stress, that was 81.41, it is clear that the dynamic factor for shear stress attenuates more slowly than that for normal stress.

Turning to the quasi-static loading condition, assuming the material's ultimate shear strength τ_{crit} is rate-independent, and incorporating the concept of the time threshold and the definition of the characteristic time, while following a similar approach for determining the maximum loading rate for flexural stress in Section 2.2.3, the maximum quasi-static loading rate for shear stress must satisfy:

$$|v| \le \frac{4\sqrt{3}}{9}\frac{1}{\xi_{\mathrm{crit}}\left(1+f^{\tau}_{\mathrm{crit}}\right)}\frac{L}{h}\frac{\tau_{\mathrm{crit}}}{\sqrt{E\rho}}. \tag{44}$$

By employing the results for the acceptable dynamic factor f^{τ}_{crit} and the time threshold ξ_{crit} in Fig. 11b, for instance, $\xi_{\mathrm{crit}} = 902.72$ and $f^{\tau}_{\mathrm{crit}} = 0.01$, the quasi-static loading rate is

$$|v| \le 0.000844\frac{L}{h}\frac{\tau_{\mathrm{crit}}}{\sqrt{E\rho}}. \tag{45}$$

2.4. Failure mode

The beam under a high loading rate is subjected to dynamic flexural and shear stresses that were derived and studied in Sections 2.2 and 2.3, respectively. Particularly for brittle materials under bending, the dominant failure mode, either flexural or shear, can be studied by defining a ratio between the maximum normal (flexural) stress ($x = 0$) and shear stress ($x \to 0$). The normal-to-shear stress ratio in terms of the characteristic time in Eq. (21) is

$$\psi(\gamma,\xi) = \lim_{x\to 0}\frac{\sigma(x,\gamma,\xi)}{\tau(x,\gamma,\xi)} = \frac{4L}{h}\left[\frac{3\xi + 2\sum_{i=1}^{\infty}\mathrm{X}_i(0,\gamma)\sin\left(\lambda_i^2\xi\right)}{3\xi - 2\sum_{i=1}^{\infty}\Lambda_i(0,\gamma)\sin\left(\lambda_i^2\xi\right)}\right]. \tag{46}$$

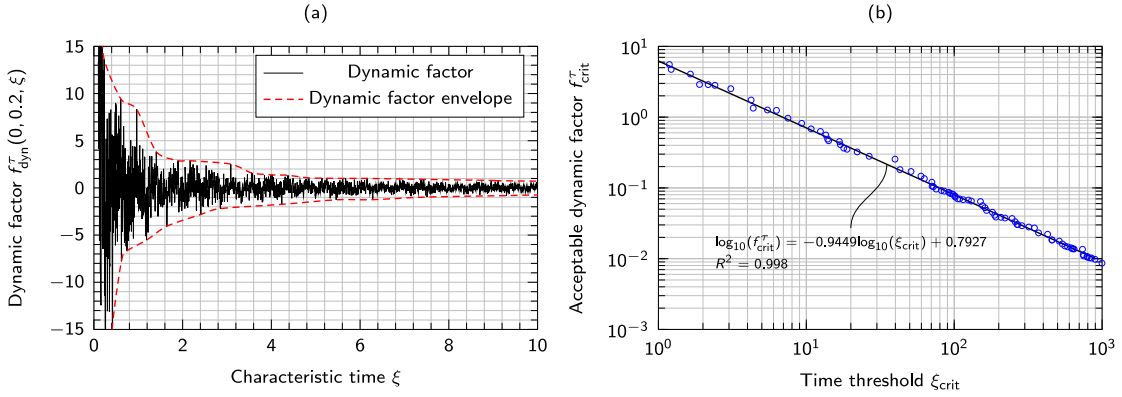

Fig. 11. (a) Dynamic factor for shear stress and its envelope; (b) relation between acceptable shear-stress dynamic factor and characteristic time threshold.

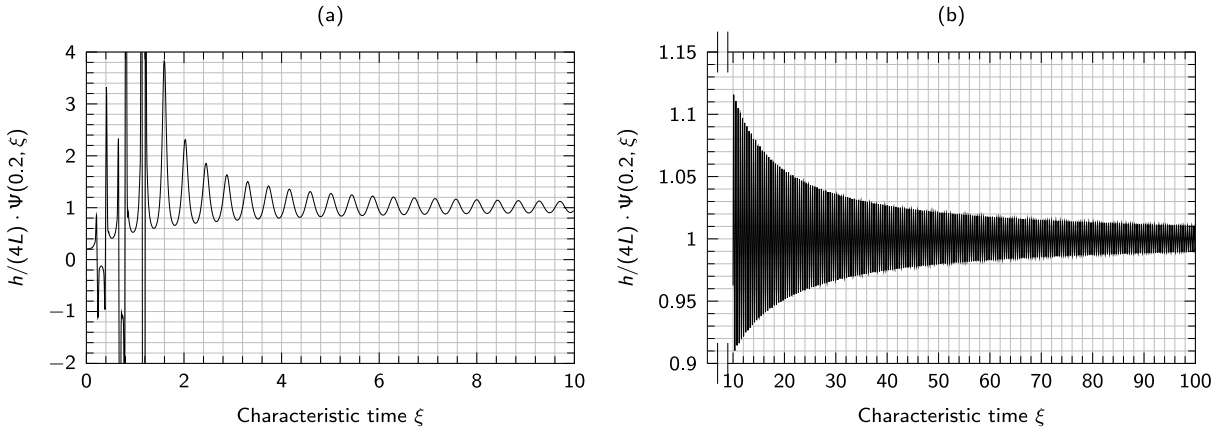

Fig. 12. Flexural-to-shear stress ratio for first vibration mode for $\gamma = 0.2$ for various characteristic times: (a) $\xi \le 10$; (b) $10 \le \xi \le 100$.

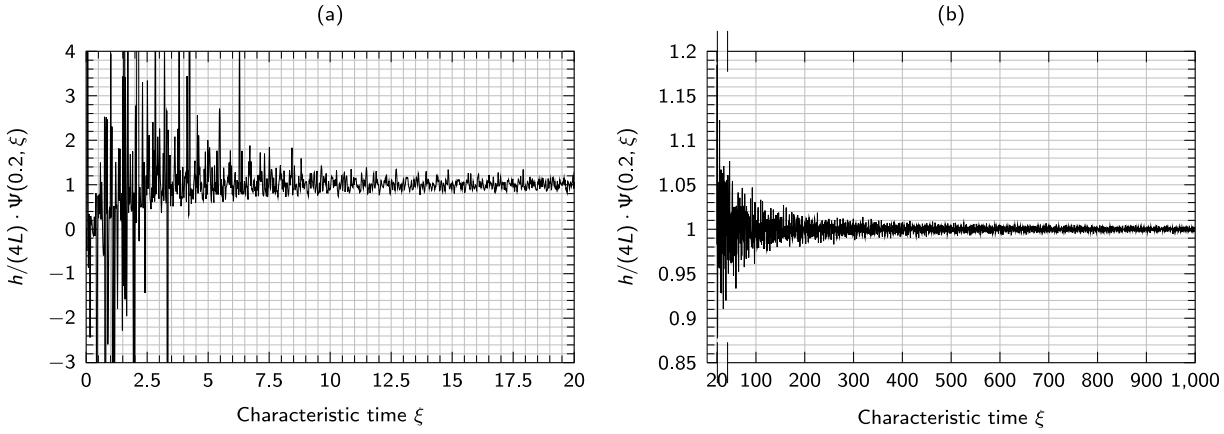

Fig. 13. Flexural-to-shear stress ratio for first ten vibration modes for $\gamma = 0.2$ for different characteristic times: (a) $\xi \le 20$; (b) $20 \le \xi \le 100$.

It is clear from Eq. (46) that the stress ratio oscillates with respect to characteristic time ξ, and, if the dynamic effect is ignored, the ratio becomes the quasi-static solution $\psi(\gamma,\xi) = 4L/h$ (note that $2L/h$ is the aspect ratio of the specimen). When the dynamic effect is significant, however, the ratio is also dependent on the beam length ratio γ.

To understand the evolution of the normal-to-shear stress ratio, the response due to the first vibration mode only is plotted against the characteristic time in Fig. 12 for $\gamma = 0.2$. Evidently, the ratio is oscillatory and can be very large for $\xi < 2$, indicating that under very high loading rates, both flexural and shear failures are possible, regardless of the specimen's aspect ratio (h/L). This means that, under dynamic loads, shear failure is possible for a long-beam configuration, and flexural failure for a short-beam configuration. By $\xi = 20$, however, the amplitude of oscillation reduces significantly, and is in the range $0.95 < h/(4L)\,\psi(0.2,\xi) < 1.05$, depending principally on the specimen's aspect ratio.

Now consider the normal-to-shear stress ratio for the first ten vibration modes (Fig. 13). The ratio oscillates more strongly with the addition of more vibration modes, and to reach the same range of $0.95 < h/(4L)\,\psi(0.2,\xi) < 1.05$, the characteristic time must be larger than 60.

2.5. Consideration of number of vibration modes

The application of the developed theory requires evaluation of the number of vibration modes. An examination can be conducted employing a modal effective mass, which provides a means to assess the significance of a mode shape and an indication of the ease to excite the vibration mode. For the beam system considered in Fig. 1b, the ith modal effective mass is

$$m_i^{\text{eff}} = \frac{\left[\int_0^L \rho A W_{1i}(x)\,dx + \int_L^{L_0} \rho A W_{2i}(x)\,dx\right]^2}{\int_0^L \rho A \left[W_{1i}(x)\right]^2 dx + \int_L^{L_0} \left[W_{2i}(x)\right]^2 dx} = \rho A \frac{\left[\int_0^L \phi_{1i}(x)\,dx + \int_L^{L_0} \phi_{2i}(x)\,dx\right]^2}{\left\{\int_0^L \left[\phi_{1i}(x)\right]^2 dx + \int_L^{L_0} \left[\phi_{2i}(x)\right]^2 dx\right\}}. \tag{47}$$

Combining the mode shapes in Eqs. (17) and (19), the dimensionless ith modal effective mass $m_i^{\text{eff}}/(\rho A L_0)$ and accumulative modal effective mass $\sum_{i=1}^{N} m_i^{\text{eff}}/(\rho A L_0)$ are plotted in Fig. 14, ($\rho A L_0$ is the total mass of the beam system in Fig. 1b).

Apparently, the dimensionless ith modal effective mass $m_i^{\text{eff}}/(\rho A L_0)$ is a function of the beam length ratio γ and when $\gamma \le 0.5$ (Fig. 14a), the first and second vibration modes are the most significant that can be excited. A convergence study can be conducted with the accumulative modal effective mass $\sum_{i=1}^{N} m_i^{\text{eff}}/(\rho A L_0)$ shown in Fig. 14b. With $N = 10$, approximate 90% of the total mass is accounted for by these first ten vibration modes. Particularly, for $\gamma = 0.2$, the dimensionless modal effective mass for the first five vibration modes are 0.406, 0.188, 0.037, 0.157 and 0.0002, respectively (Fig. 14a), making nearly 80% of the total mass (Fig. 14b).

Another upper constraint on the number of vibration mode being considered is due to the inherent limitations of the Euler–Bernoulli beam theory. In this theory, the phase speed of the ith vibration mode flexural wave is $C_i^{\text{p}} = \omega_i/\beta_i = (\lambda_i/L)\sqrt{EI/(\rho A)}$, which can become infinitely large with the increasing eigenvalue λ_i. Generally, without generating a shock wave, the phase speed C_i^{p} should be smaller than

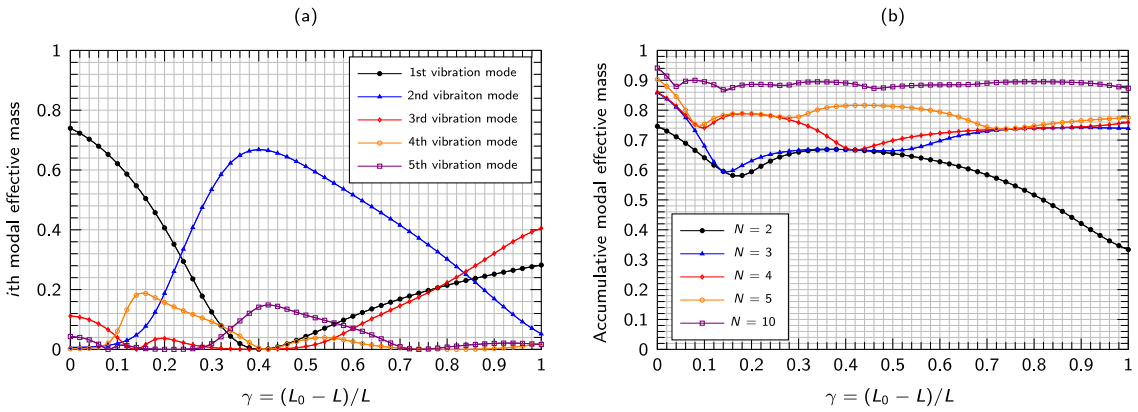

Fig. 14. (a) *i*th modal effective mass; (b) accumulative modal effective mass.

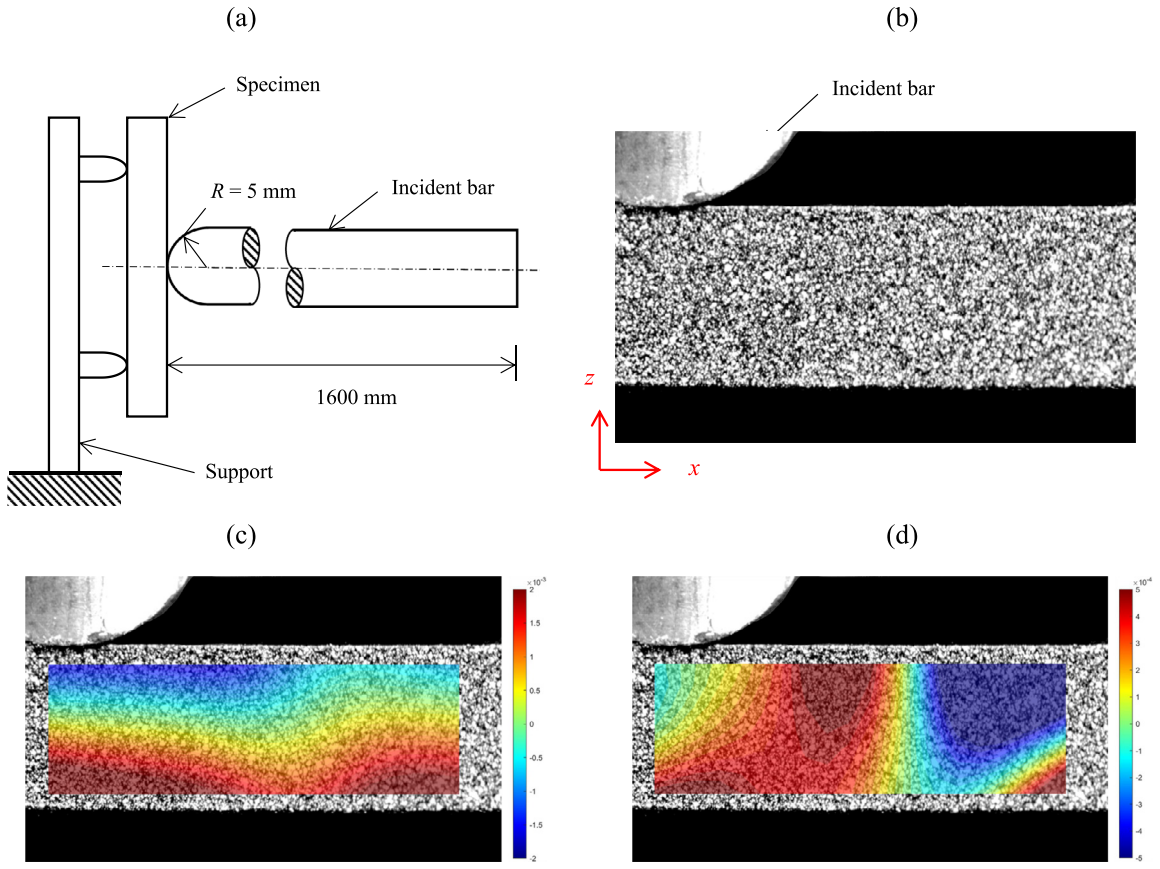

Fig. 15. (a) Schematic of split Hopkinson bar experimental setup; (b) specimen with speckles. Typical DIC data for normal (c) and shear (d) strains at 0.175 ms.

the dilatational wave speed $\sqrt{E/\rho}$, providing the upper limit for the number of vibration modes with eigenvalues $\lambda_i \leq 2\sqrt{3}(L/h)$.

3. Experimental and numerical verifications

3.1. Experimental verification

Experimental verification of the developed theory was conducted on Ti6Al4V specimens using split Hopkinson bar (SHB) impact test. The geometry of the Ti6Al4V specimen was: $2L_0 = 200$ mm, $2L = 165$ mm, (giving a length ratio γ of approximately 0.21), thickness $h = 5.44$ mm and width $b = 20$ mm. Three specimens were tested under the SHB impact. The Young's modulus of Ti6Al4V is 113.8 GPa and the Poisson ratio is 0.342 according to the manufacturer's datasheet.

The specimen during the impact was filmed with a high-speed camera with a resolution of 512 × 304 pixels at a frame rate of 80 000 fps. Then, the filmed images were post-processed, employing a digital image correlation (DIC) method to derive the normal and shear strains to verify the theoretical development in Section 2. The schematic of the experimental setup is shown in Fig. 15a with the specimen resting on two supports, while the specimen with speckles is in Fig. 15b. The typical DIC results for normal and shear strains are in Fig. 14c and d, respectively.

For the analytical results, the normal strain $\epsilon_{xx}(x,z,t)$ and shear strain $\epsilon_{xz}(x,z,t)$, according to Eqs. (28) and (40), are calculated using

$$\epsilon_{xx}(x,z,t) = \left[4\sqrt{3}v\sqrt{\frac{E}{\rho}}\sum_{i=1}^{\infty}\mathrm{X}_i(x,\gamma)\sin(\omega_i t) + \left(1-\frac{1}{L}x\right)\frac{3hvt}{L^2}\right]\frac{z}{h}, \tag{48}$$

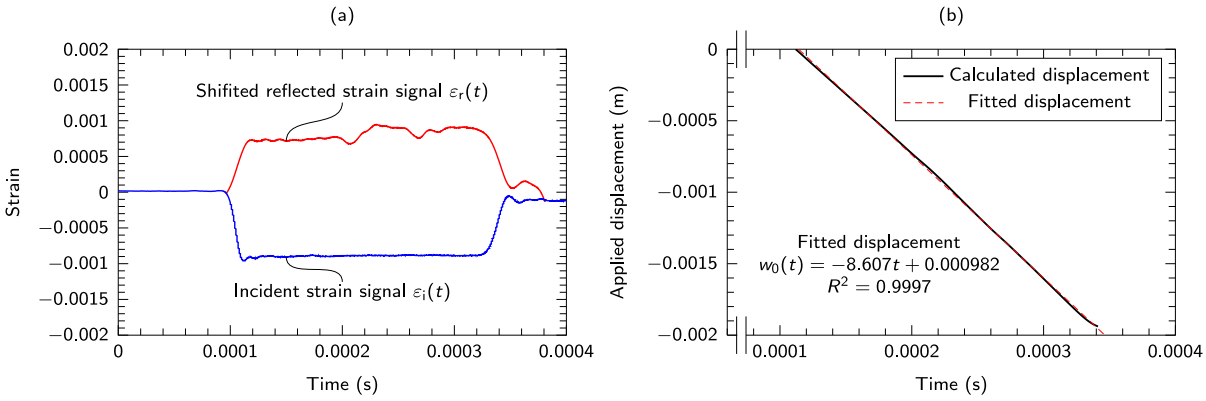

Fig. 16. (a) Incident and shifted reflected strain signals; (b) calculated applied displacement.

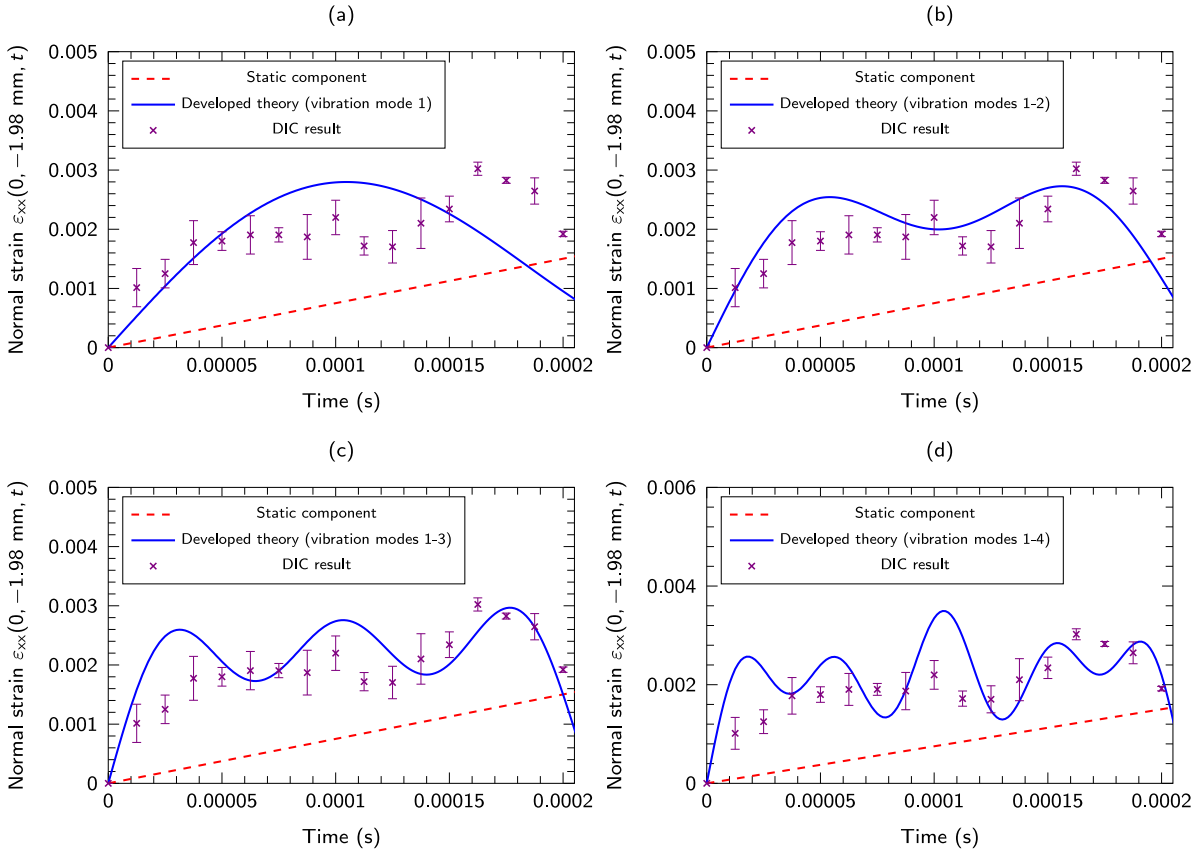

Fig. 17. Comparison of normal-strain results from developed theory and DIC results for first (a), first two (b), first three (c) and first four (d) vibration modes for point (0, −1.98 mm).

$$\varepsilon_{xz}(x,z,t) = \left[-4\sqrt{3}\frac{h}{L}v(1+\nu)\sqrt{\frac{\rho}{E}}\sum_{i=1}^{\infty}\Lambda_i(x,\gamma)\sin(\omega_i t) + (1+\nu)\frac{3h^2 vt}{L^3}\right] \times \left(\frac{1}{4} - \frac{z^2}{h^2}\right), \tag{49}$$

The loading rate v is obtained by the applied displacement $w_0(t)$, which was derived by processing the incident and shifted reflected strain signals employing Eq. (50), where $\varepsilon_i(t)$ and $\varepsilon_r(t)$ are the incident and shifted reflected strain signals and C_0 is the longitudinal wave speed of the incident bar [49].

$$w_0(t) = -C_0 \int \left[\varepsilon_r(t) - \varepsilon_i(t)\right] dt\,. \tag{50}$$

The strain signals are presented in Fig. 16a, while the calculated applied displacement is in Fig. 16b with the fitted displacement, giving a loading rate of 8.61 m s^{-1}.

The normal strain verification was conducted for point of (0, −1.98 mm), the analytical solution with increasing vibration mode number up to 4 are compared with the DIC results (with standard deviation as error bars) together with the quasi-static component in Fig. 17.

It is seen that the normal strain obtained with the DIC method is oscillatory (Fig. 17), and the analytical results capture this oscillatory nature; by adding more modes up to the third vibration modes, the analytical solution becomes increasingly closer to the DIC results, but

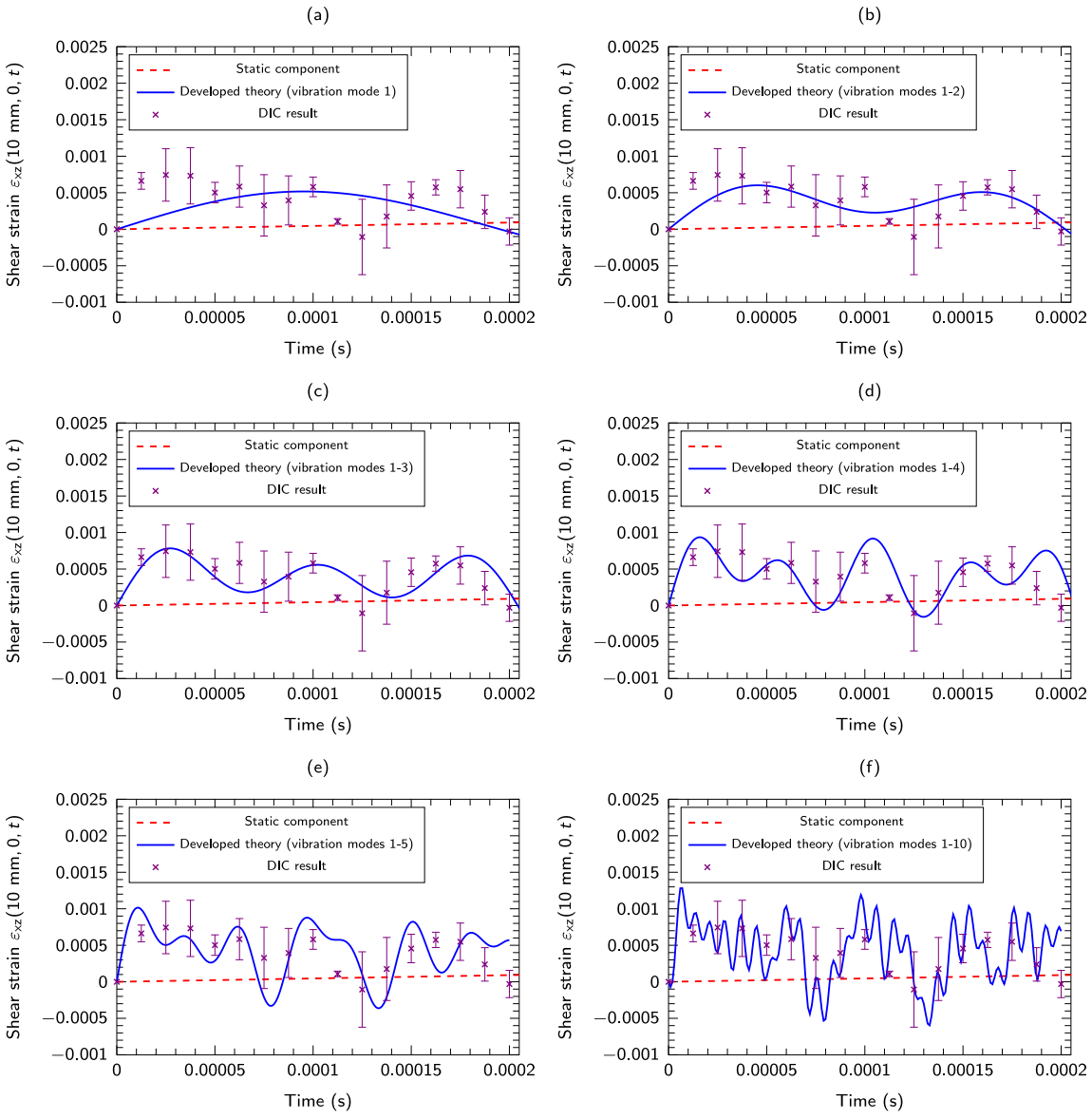

Fig. 18. Comparison of shear strain results from developed theory and DIC results for first (a), first two (b), first three (c), first four (d), first five (e) and first ten (f) vibration modes for point (10 mm, 0).

not after the fourth vibration mode. This is due to the phenomenon known as *loss-of-contact* [50] that after the initial impact the specimen bounces off the supports for a brief period, giving an immediate load relief, and some of higher vibration modes might not be properly excited and represented. This can also be referred to the findings in Section 2.5 that the first four vibration modes make up nearly 80% of the total mass of the beam system in Fig. 1b, and the analytical result with these vibration modes is already comparable to the DIC results. In addition, this loss-of-contact also alters the boundary conditions, and, according to Fig. 2b, the frequencies of higher vibration modes are more susceptible to boundary-condition change, and the prediction of their frequencies might not be as accurate.

Turning to the comparison of shear strain between the analytical and DIC results, the point (10 mm, 0) was chosen, and comparisons with various vibration modes are given in Fig. 18. For the mean value of DIC shear strain results, the analytical solution is in a good agreement with the first three vibration modes. But the standard deviation of the shear strain results is larger than that for the normal strain (Fig. 17), showing a considerable contribution from the higher vibration modes; as seen in Fig. 18f, when first ten vibration modes are considered, the deviation of the DIC results is in accordance with variation of the oscillating analytical results.

3.2. Numerical verification

Experimental verification shows a good agreement between the results of the analytical analysis and the DIC data, but for this high dynamic event, the latter are limited by the capability of the high-speed camera. A further numerical verification is conducted with finite-element-method (FEM) simulations. A 2D FEM model was built in Abaqus/Explicit using four-node plane-stress elements (CPS4R) with a uniform element size of 0.1 mm after a mesh convergence study. Note that in the FEM model the constitutive model for the material is elastic, with linear bulk viscosity set to zero, in accordance with the analytical theory developed in Section 2 without consideration of the damping effect. The dynamic normal stress $\sigma(0, -h/2, t)$ at lower surface of $x = 0$ was extracted and compared to the analytical solutions for various vibration modes (Fig. 19).

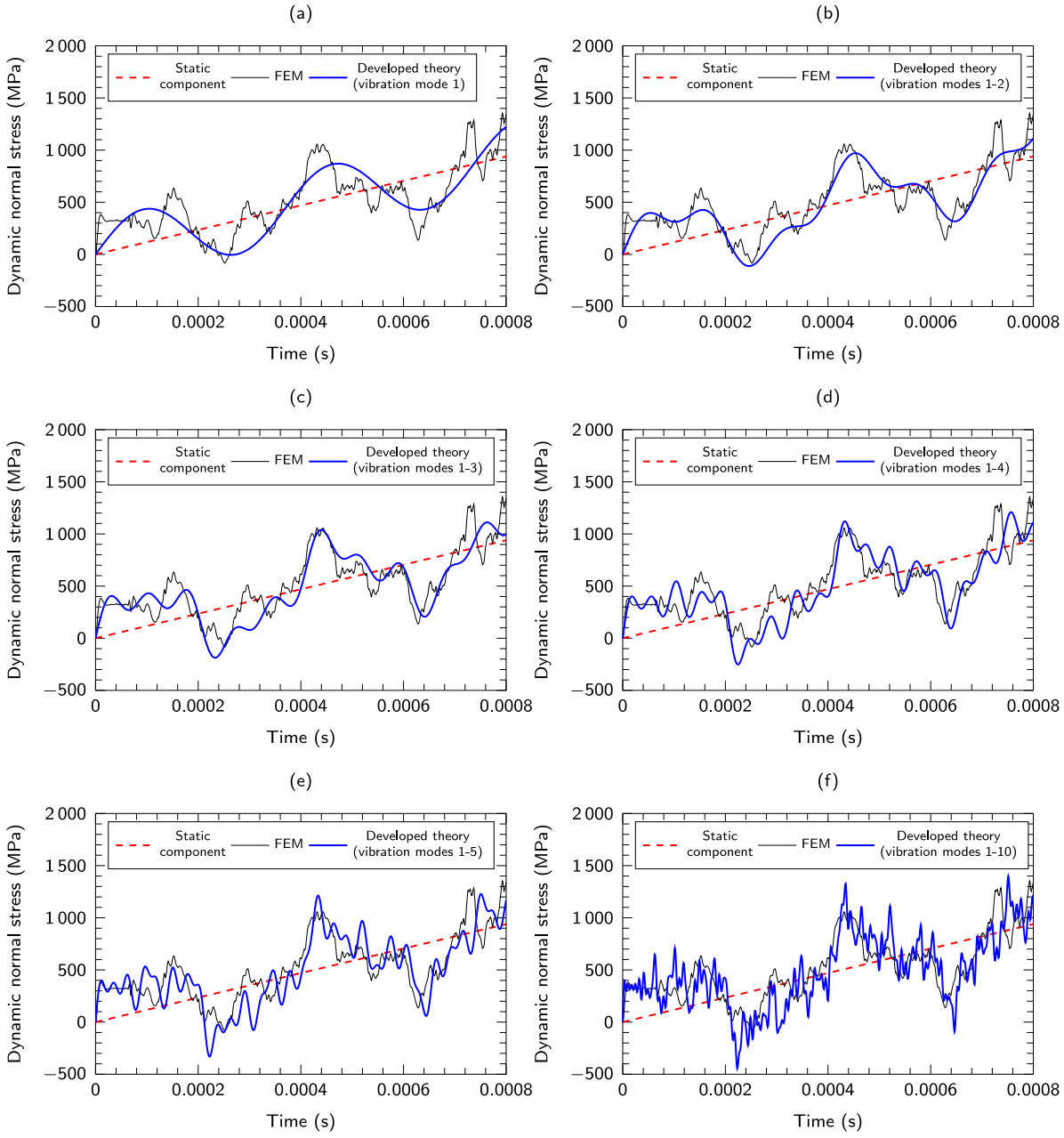

Fig. 19. Evolution of dynamic flexural stress obtained with developed theory and FEM for increasing numbers of vibration modes at $(0, -h/2)$: first (a), first two (b), first three (c), first four (d), first five (e) and first ten (f) vibration modes.

As shown in Fig. 19, the dynamic normal stress determined with the developed theory is in good agreement with FEM results, especially for lower vibration modes similar to the finding of experimental verification; with adding more vibration modes the magnitudes of normal stress predicted by the developed theory becomes increasingly close to the FEM results. This agreement can be further examined by comparing the results of Fast Fourier Transform (FFT), which provides a quantitative assessment of the agreement as shown in Fig. 20.

As demonstrated by Fig. 20, the analytical results are more accurate for the first three vibration modes. In the FEM results, the amplitudes of the fourth and fifth vibration modes are barely visible due to the phenomenon of loss-of-contact, confirming the finding of the experimental verification in Section 3.1.

The comparisons for shear stress at (10 mm, 0) are given in Fig. 21, considering both the phase and amplitude of each vibration mode. Moreover, the analytical solution becomes increasingly close to the FEM results with adding more vibration modes. It is worth noting that the maximum value of the shear-stress component due to quasi-static motion τ_{sta} is 15.49 MPa at 0.0008 s, but the maximum value of the shear stress component due to structural vibration τ_{vib} can be as high as 80.53 MPa, giving a total dynamic shear stress of 89.97 MPa. This demonstrates that at high loading rate, shear failure can happen considerably earlier than the displacement reaches the critical value for the quasi-static shear failure. A quantitative assessment of the agreement between the analytical and FEM results was also conducted with the FFT method, and the detailed comparison is in Fig. 22, with findings similar to those for the normal stress.

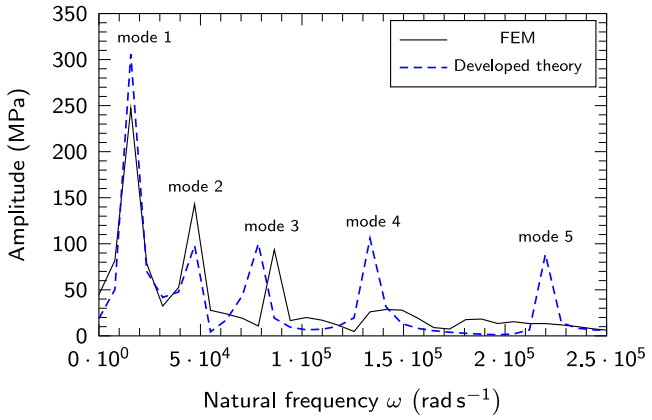

Fig. 20. Comparison of FFT results for developed theory and FEM.

4. Conclusion

The theory of dynamic three-point bending under high-loading rates was developed, providing analytical solutions for assessment of the dynamic normal (flexural) and shear stresses, which was then verified by experiments and numerical simulations. Generally, under high loading rates, the dynamic effect, which is quantified and studied in terms of dynamic factors and a dimensionless characteristic time, can be significant. It was found that the dynamic effect attenuated very quickly with characteristic time ξ, employed to determine the quasi-static time thresholds: for normal stress, $\xi > \xi_{crit} = 81.41$, and for shear stress, $\xi > \xi_{crit} = 902.72$, the dynamic effect can be considered insignificant. In addition, the quasi-static loading conditions were investigated for both normal and shear stresses, and the critical loading rates were obtained, below which the dynamic effect is insignificant (less than 1%).

The dominant failure mode in dynamic bending was also studied for brittle materials. It was found that at $\xi < 10$, the normal-to-shear stress

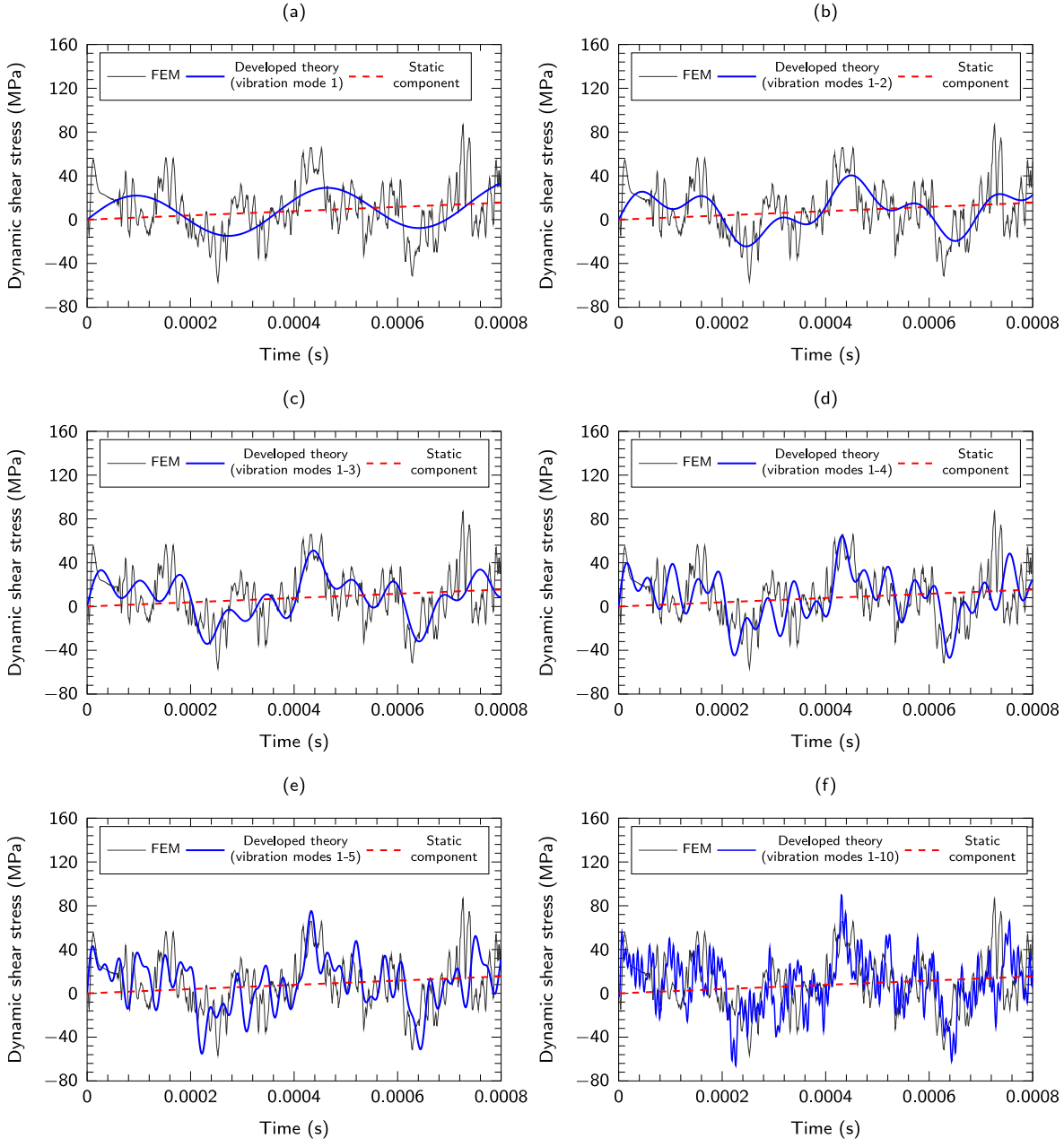

Fig. 21. Evolution of dynamic shear stress obtained with developed theory and FEM for increasing numbers of vibration modes at (10 mm, 0): first (a), first two (b), first three (c), first four (d), first five (e) and first ten (f) vibration modes.

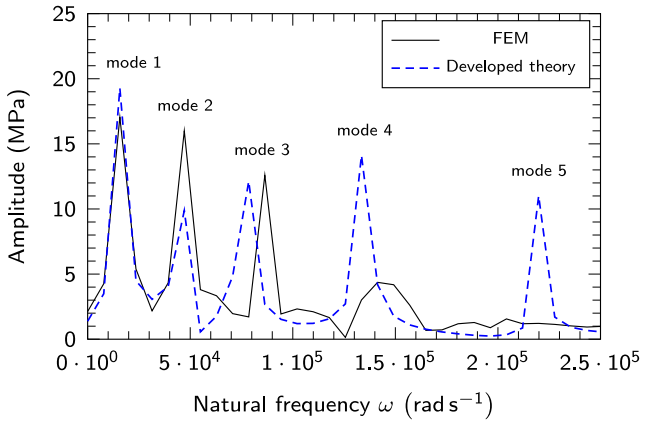

Fig. 22. Comparison of FFT results for developed theory and FEM.

ratio oscillates, but beyond this time, the dominant failure mode was determined by the specimen's geometry alone, depending on its ratio $4L/h$.

The developed theory was verified experimentally with DIC strain results for a dynamic three-bending test of Ti6Al4V under the split Hopkinson bar impact. It was demonstrated that although the specimen experienced some loss of contact, the analytical solutions with lower vibration modes still provided the accurate results. Further numerical verification confirmed this and also showed that for both normal and shear stresses, with addition of more vibration modes, the analytical results became increasingly closer to the FEM results in terms of the overall magnitude, although the frequencies of higher vibration modes were less accurate.

CRediT authorship contribution statement

Tianyu Chen: Writing – original draft, Validation, Formal analysis, Conceptualization. **Quanyu Jiang:** Validation, Investigation, Data curation. **Jian Xue:** Visualization, Methodology, Formal analysis. **Christopher M. Harvey:** Writing – review & editing, Formal analysis, Conceptualization. **Xiang Zhang:** Writing – review & editing, Visualization, Methodology. **Vadim V. Silberschmidt:** Writing – review & editing, Methodology. **Yiding Liu:** Validation, Investigation. **Kun Zhang:** Visualization, Methodology, Funding acquisition, Conceptualization. **Simon Wang:** Writing – review & editing, Visualization. **Bingchen Wei:** Supervision, Resources, Project administration, Funding acquisition.

Declaration of competing interest

The authors declare that they have no known competing financial interests or personal relationships that could have appeared to influence the work reported in this paper.

Data availability

No data was used for the research described in the article

Acknowledgments

This work was supported by the National Natural Science Foundation of China (Grant No. 12272392 No.11790292). All authors read and approved the final manuscript.

Appendix A. Mode shape comparison for symmetric and asymmetric configurations

See Fig. A.1

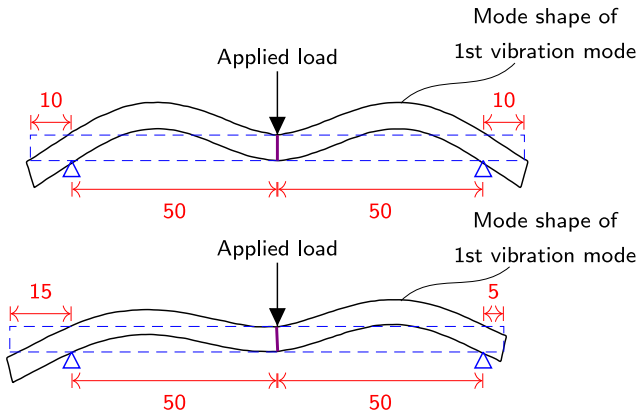

Fig. A.1. Comparison of mode shapes for symmetric and asymmetric configurations.

Appendix B. Boundary conditions and continuity conditions

Employing the deflection assumptions in Eqs. (3) and (4) and forcing the homogeneous conditions together with the boundary conditions for total deflections of beam sections ① and ②, the boundary conditions for $w_{1\mathrm{fv}}(x,t)$ and $F_1(x)$ can be determined and they are given in Table B.1, while the boundary conditions for $w_{2\mathrm{fv}}(x,t)$ and $F_2(x)$ are in Table B.2, and continuity conditions are in Table B.3.

Appendix C. Derivation of orthogonality condition

The orthogonality condition can be derived as follows: multiplying Eq. (13) by $W_{1j}(x)$, integrating twice by parts over the length of beam section ① from 0 to L, applying the boundary conditions in Table B.1 to have

$$\omega_i^2 \frac{\rho A}{EI} \int_0^L W_{1i}(x) W_{1j}(x)\, dx = -W_{1j}^{(1)}(L) W_{1i}^{(2)}(L) + \int_0^L W_{1i}^{(2)}(x) W_{1j}^{(2)}(x)\, dx. \tag{C.1}$$

Similarly, for beam section ②, multiplying Eq. (14) by $W_{2j}(x)$, integrating twice by parts over the beam section length from L to L_0, applying the boundary conditions in Table B.2 to obtain

$$\omega_i^2 \frac{\rho A}{EI} \int_L^{L_0} W_{2i}(x) W_{2j}(x)\, dx = W_{2j}^{(1)}(L) W_{2i}^{(2)}(L) + \int_L^{L_0} W_{2i}^{(2)}(x) W_{2j}^{(2)}(x)\, dx. \tag{C.2}$$

.

Adding Eqs. (C.1) and (C.2) and subtracting the result with i and j exchanged to have

$$\left(\omega_i^2 - \omega_j^2\right) \frac{\rho A}{EI} \left[\int_0^L W_{1i}(x) W_{1j}(x)\, dx + \int_L^{L_0} W_{2i}(x) W_{2j}(x)\, dx\right] = 0. \tag{C.3}$$

Since the natural frequency is unique, that is, $\omega_i \neq \omega_j$ for $i \neq j$, and, therefore,

$$\frac{\rho A}{EI} \left[\int_0^L W_{1i}(x) W_{1j}(x)\, dx + \int_L^{L_0} W_{2i}(x) W_{2j}(x)\, dx\right] = 0. \tag{C.4}$$

Including the case of $i = j$, the orthogonality condition is found to be

$$\frac{\rho A}{EI} \left[\int_0^L W_{1i}(x) W_{1j}(x)\, dx + \int_L^{L_0} W_{2i}(x) W_{2j}(x)\, dx\right] = \delta_{ij}. \tag{C.5}$$

Table B.1
Boundary conditions for beam section ①.

Boundary	Total deflection $w_1(x,t)$	Free-vibration component $w_{1\mathrm{fv}}(x,t)$	Normal mode $W_{1i}(x)$	Shifting function $F_1(x)$
$x=0$	$w(0,t)=vt$	$w_{\mathrm{fv}}(0,t)=0$	$W_{1i}(0)=0$	$F(0)=1$
	$w^{(1)}(0,t)=0$	$w^{(1)}_{\mathrm{fv}}(0,t)=0$	$W^{(1)}_{1i}(0)=0$	$F^{(1)}(0)=0$
$x=L$	$w(L,t)=0$	$w_{\mathrm{fv}}(L,t)=0$	$W_{1i}(L)=0$	$F(L)=0$

Table B.2
Boundary conditions for beam section ②.

Boundary	Total deflection $w_2(x,t)$	Free-vibration component $w_{2\mathrm{fv}}(x,t)$	Normal mode $W_{2i}(x)$	Shifting function $F_2(x)$
$x=L$	$w_2(L,t)=0$	$w_{2\mathrm{fv}}(L,t)=0$	$W_{2i}(L)=0$	$F_2(L)=0$
$x=L_0$	$EIw^{(2)}_2(L_0,t)=0$	$EIw^{(2)}_{2\mathrm{fv}}(L_0,t)=0$	$W^{(2)}_{2i}(L_0)=0$	$EIF^{(2)}_2(L_0)=0$
	$EIw^{(3)}_2(L_0,t)=0$	$EIw^{(3)}_{2\mathrm{fv}}(L_0,t)=0$	$W^{(3)}_{2i}(L_0)=0$	$EIF^{(3)}_2(L_0)=0$

Table B.3
Continuity conditions.

	Total deflection	Free-vibration component	Shifting function
Deflection	$w_1(L,t)=w_2(L,t)$	$w_{1\mathrm{fv}}(L,t)=w_{2\mathrm{fv}}(L,t)$	$F_1(L)=F_2(L)$
Slope	$w^{(1)}_1(L,t)=w^{(1)}_2(L,t)$	$w^{(1)}_{1\mathrm{fv}}(L,t)=w^{(1)}_{2\mathrm{fv}}(L,t)$	$F^{(1)}_1(L)=F^{(1)}_2(L)$
Bending moment	$w^{(2)}_1(L,t)=w^{(2)}_2(L,t)$	$w^{(2)}_{1\mathrm{fv}}(L,t)=w^{(2)}_{2\mathrm{fv}}(L,t)$	$F^{(2)}_1(L)=F^{(2)}_2(L)$

Appendix D. Derivation of initial modal displacement and velocity

The initial displacement of beam sections ① and ②, according to Eqs. (11) and (12), are

$$w_{1\mathrm{fv}}(x,0)=\sum_{i=1}^{\infty}W_{1i}(x)\,T_i(0), \tag{D.1}$$

$$w_{2\mathrm{fv}}(x,0)=\sum_{i=1}^{\infty}W_{2i}(x)\,T_i(0). \tag{D.2}$$

Multiplying Eq. (D.1) by $\rho AW_{1j}(x)/(EI)$ and multiplying Eq. (D.2) by $\rho AW_{2j}(x)/(EI)$, adding their products and applying the orthogonality condition in Eq. (C.5) to have

$$T_i(0)=\frac{\rho A}{EI}\left[\int_0^{L}W_{1i}(x)\,w_{1\mathrm{fv}}(x,0)\,dx+\int_L^{L_0}W_{2i}(x)\,w_{2\mathrm{fv}}(x,0)\,dx\right]. \tag{D.3}$$

Similarly, the initial modal velocity is

$$\dot{T}_i(0)=\frac{\rho A}{EI}\left[\int_0^{L}W_{1i}(x)\,\dot{w}_{1\mathrm{fv}}(x,0)\,dx+\int_L^{L_0}W_{2i}(x)\,\dot{w}_{2\mathrm{fv}}(x,0)\,dx\right]. \tag{D.4}$$

Appendix E. Simplification of initial modal velocity

Substituting $\dot{w}_{1\mathrm{fv}}(0,t)=-vF_1(x)$, $\dot{w}_{2\mathrm{fv}}(0,t)=-vF_2(x)$, $W_{1i}(x)=W^{(4)}_{1i}(x)/\beta_i^4$ (Eq. (13)) and $W_{2i}(x)=W^{(4)}_{2i}(x)/\beta_i^4$ (Eq. (14)) into Eq. (24), and, then, integrating by parts four times together with the boundary conditions in Table B.1 and Table B.2 and the continuity conditions in Table B.3, the initial modal velocity is simplified to

$$\dot{T}_i(0)=v\frac{1}{\omega_i^2}W^{(3)}_{1i}(0). \tag{E.1}$$

References

[1] H. Hu, et al., Characterization of progressive damage behaviour and failure mechanism of carbon fibre reinforced DP590 laminates, Thin-Walled Struct. 168 (2021) 108293.

[2] R.A. Aleaimat, et al., Behaviour of square concrete filled FRP tube columns under concentric, uniaxial eccentric, biaxial eccentric and four-pint bending loads, Thin-Walled Struct. 168 (2021) 108252.

[3] J. Zhang, et al., Failure behavior of a sandwich beam with GLARE face-sheets and aluminum foam core under three-point bending, Thin-Walled Struct. 183 (2023) 110438.

[4] S.B. Ali, et al., Concrete-filled and bare 6082-T6 aluminium alloy tubes under in-plane bending: Experiments, finite element analysis and design recommendations, Thin-Walled Struct. 172 (2022) 108907.

[5] J. Zhang, et al., Failure behavior of sandwich beams with glass fiber-reinforced epoxy/aluminum laminates face-sheets and aluminum honeycomb core under three-point bending, Thin-Walled Struct. 177 (2022) 109476.

[6] Z. Zhang, et al., Failure analysis of brazed sandwich structures with square honeycomb-corrugation hybrid cores under three-point bending, Thin-Walled Struct. 170 (2022) 108591.

[7] G.A.O. Davies, X. Zhang, Impact damage prediction in carbon composite structures, Int. J. Impact Eng. 16 (1995) 149–170.

[8] C. Yin, D. Terentyev, et al., Ductile to brittle transition in ITER specification tungsten assessed by combined fracture toughness and bending tests analysis, Mater. Sci. Eng. A 750 (2019) 20–30.

[9] M.A. Caminero, G.P. Rodriguez, V. Munoz, Effect of stacking sequence on charpy impact and flexural damage behavior of composite laminates, Compos. Struct. 136 (2016) 345–357.

[10] B. Tang, et al., Numerical modeling of ductile fracture of hot stamped 22MnB5 boron steel parts in three-point bending, Int. J. Mech. Sci. 188 (2022) 105951.

[11] A. Liens, M. Swain, et al., Development of transformation bands in ceria-stabilized-zirconia based composites during bending at room temperature, J. Eur. Ceram. Soc. 23 (2003) 1987–1996.

[12] S. Gao, et al., Experimental investigation on bending behavior of ZrO2 honeycomb sandwich structures prepared by DLP stereolithography, Thin-Walled Struct. 157 (2020) 107099.

[13] D. Tscharnuter, S. Gastl, G. Pinter, Modeling of the nonlinear viscoelasticity of polyoxymethylene in tension and compression, Internat. J. Engrg. Sci. 60 (2012) 37–52.

[14] F. Li, F. Scarpa, et al., Bending shape recovery of unidirectional carbon fiber reinforced epoxy-based shape memory polymer composites, Composites A 116 (2019) 169–179.

[15] A. Makeev, S. Ghaffari, G. Seon, Improving compressive strength of high modulus carbon-fiber reinforced polymeric composites through fiber hybridization, Internat. J. Engrg. Sci. 412 (2019) 145–157.

[16] T. Wu, et al., Flexural properties of electrothermal deicing composite laminates: experimental and numerical study, Thin-Walled Struct. 170 (2022) 108527.

[17] S.P. Mai, N.A. Fleck, T.J. Lu, Optimal design of box-section sandwich beams in three-point bending, Int. J. Solids Struct. 44 (2007) 4742–4769.

[18] Y. Li, et al., Behaviour of seawater and sea sand concrete filled FRP square hollow sections, Thin-Walled Struct. 148 (2020) 106596.

[19] Y. Zhu, Y. Sun, Low-velocity impact response of multilayer foam core sandwich panels with composite face sheet, Int. J. Mech. Sci. 2009 (2021) 106704.

[20] Y. Lin, et al., Characterization of progressive damage behavior and failure mechanisms of carbon fibre reinforced aluminium laminates under three-point bending, Thin-Walled Struct. 135 (2019) 494–506.

[21] Y. Qureshi, M. Tarfaoui, et al., Development of microscale flexible nylon/Ag strain sensor wire for real-time monitoring and damage detection in composite structures subjected to three-point bend test, Compos. Sci. Technol. 181 (2019) 107693.
[22] Y.N. Butusova, V.V. Mishakin. M. Kachanov, On monitoring the incubation stage of stress corrosion cracking in steel by the eddy current method, Internat. J. Engrg. Sci. 148 (2020) 103212.
[23] X. Zhao, et al., Effects of porosity and flexoelectricity on static bending and free vibration of AFG piezoelectric nanobeams, Thin-Walled Struct. 151 (2020) 106754.
[24] ASTM C393, Standard test method for core shear properties of sandwich constructions by beam flexure.
[25] ASTM C1161, Standard test method for flexural strength of advanced ceramics at ambient temperature.
[26] ASTM C1609, Standard test method for flexural performance of fiber-reinforced concrete (using beam with third-point loading).
[27] ASTM D790, Standard test methods for flexural properties of unreinforced and reinforced plastics and electrical insulting materials.
[28] ASTM D2344, Standard test method for short-beam strength of polymer matrix composite materials and their laminates.
[29] ASTM D7264, Standard test method for flexural properties of polymer matrix composite materials.
[30] ASTM E290, Standard test methods for bend testing of material for ductility.
[31] Y. Xiao, et al., Dynamic bending responses of CFRP thin-walled square beams filled with aluminum honeycomb, Thin-Walled Struct. 132 (2018) 494–503.
[32] Z. Huang, et al., A comparative study on the energy absorption mechanism of aluminum/CFRP hybrid beams under quasi-static and dynamic bending, Thin-Walled Struct. 163 (2021) 107772.
[33] V. Crupi, R. Montanini, Aluminium foam sandwiches collapse modes under static and dynamic three-point bending, Int. J. Impact Eng. 34 (2007) 509–521.
[34] G. Zhou, Q. Sun, et al., Crushing behaviors of unidirectional carbon fiber reinforced plastic composites under dynamic bending and axial crushing loading, Int. J. Impact Eng. 140 (2020) 103539.
[35] B. Koohbor, A. Kidane, et al., Analysis of dynamic bending test using ultra high speed DIC and the virtual fields method, Int. J. Impact Eng. 110 (2017) 299–310.
[36] A. Ruhl, S. Kolling, J. Schneider, A transparent three-layered laminate composed of poly(methyl methacrylate) and thermoplastic polyurethane subjected to low-velocity impact, Int. J. Impact Eng. 136 (2020) 103419.
[37] G.A.O. Davies, R. Olsson, Impact on composite structures, Aeronaut. J. 108 (2004) 541–563.
[38] F. Delvare, J.L. Hanus, P. Bailly, A non-equilibrium approach to processing hopkinson bar bending test data: Application to quasi-brittle materials, Int. J. Impact Eng. 37 (2010) 1170–1179.
[39] M. Dan, et al., Free vibration analysis of simply supported beams with solid and thin-walled cross-sections using higher-order theories based on displacement variables, Thin-Walled Struct. 98 (2016) 478–495.
[40] Z. Wu, et al., Effect of stacking configuration on the mechanical property and damage behavior of braided property and damage behavior of braided composite tube under three-point bending, Thin-Walled Struct. 187 (2023) 110762.
[41] J. Chen, et al., Experimental and analytical study of hollow section concrete-filled GFRP tubes in bending, Thin-Walled Struct. 177 (2022) 109297.
[42] D. Rincon-Davila, et al., Theoretical-experimental study of the bending behavior of thin-walled rectangular tubes, Thin-Walled Struct. 173 (2022) 109009.
[43] B. Li, et al., 7A04-T6 high-strength aluminium alloy SHS and RHS beams under pure bending – testing, modelling and design recommendations, Thin-Walled Struct. 177 (2022) 109400.
[44] H. Yuan, et al., The failure behavior of double-layer metal foam sandwich beams under three-pint bending, Thin-Walled Struct. 180 (2022) 109801.
[45] F. Xia, et al., Three-point bending performance of sandwich panels with various types of cores, Thin-Walled Struct. 179 (2022) 109723.
[46] A. Nguyen, Experimental investigation of roll-formed aluminium lipped channel beams subjected to combined bending and web crippling, Thin-Walled Struct. 171 (2022) 108804.
[47] E. Georgantzia, et al., Design of aluminium alloy channel sections under minor axis bending, Thin-Walled Struct. 174 (2022) 109098.
[48] H. Yin, et al., On bending crashworthiness of smooth-shell lattice-filled structures, Thin-Walled Struct. 171 (2022) 108800.
[49] H. Liu, H. Nie, C. Zhang, Y. Li, Loading rate dependency of mode I interlaminar fracture toughness for unidirectional composite laminates, Compos. Sci. Technol. 167 (2018) 215–223.
[50] F. Jiang, K.S. Vecchio, Hopkinson bar loaded fracture experimental technique: A critical review of dynamic fracture toughness tests, Appl. Mech. Rev. 62 (2009) 060802.